Title: The molecular infrastructure of glutamatergic synapses in the mammalian forebrain

Authors:

J. Peukes[1,2], C. Lovatt[3,4], C. Leistner[3,5], J. Boulanger[1], D. R. Morado[1,6], M. J. G. Fuller[3], W. Kukulski[1,7], F. Zhu[8], N. H. Komiyama[8,9], J. A. G. Briggs[1,10], S. G. N. Grant[8], R. Frank[1,3*]

Affiliations:

[1] MRC Laboratory of Molecular Biology, Francis Crick Avenue, Cambridge, CB2 0QH, UK.

[2] Current address: University of California Berkeley, QB3, Berkeley, USA

[3] Astbury Centre for Structural Molecular Biology, School of Biomedical Sciences, Faculty of Biological Sciences, University of Leeds, LS2 9JT, UK.

[4] Current address: Rosalind Franklin Institute, Didcot, OX11 0QS, UK.

[5] Current address: Harvard Medical School

[6] Current address: Science for Life Laboratory, Department of Biochemistry and Biophysics, Stockholm University, 17165 Solna, Sweden.

[7] Current address: Institute of Biochemistry and Molecular Medicine, University of Bern, 3012 Bern, Switzerland.

[8] Genes to Cognition Program, Centre for Clinical Brain Sciences, Simons Initiative for the Developing Brain, University of Edinburgh, Edinburgh EH16 4SB, UK.

[9] Genes to Cognition Program, Centre for Clinical Brain Sciences, Simons Initiative for the Developing Brain, the Muir Maxwell Epilepsy Centre, University of Edinburgh, Edinburgh EH16 4SB, UK.

24 [10] Current Address: Max Planck Institute of Biochemistry, Martinsried, Germany.

25 * Corresponding author. Email: r.frank@leeds.ac.uk

26 **Abstract**

27 Glutamatergic synapses form the vast majority of connections within neuronal circuits, but
28 how these subcellular structures are molecularly organized within the mammalian brain is
29 poorly understood. Conventional electron microscopy using chemically fixed, metal-
30 stained tissue has identified a proteinaceous, membrane-associated thickening called the
31 'postsynaptic density' (PSD). Here, we combined mouse genetics and cryo-electron
32 tomography to determine the 3D molecular architecture of fresh isolated and anatomically
33 intact synapses in the adult forebrain. The native glutamatergic synapse did not consistently
34 show a higher density of proteins at the postsynaptic membrane thought to be characteristic
35 of the PSD. Instead, a 'synaptoplasm' consisting of cytoskeletal elements, macromolecular
36 complexes and membrane-bound organelles extended throughout the pre- and post-
37 synaptic compartments. Snapshots of active processes gave insights into membrane
38 remodeling processes. Clusters of up to 60 ionotropic glutamate receptors were positioned
39 inside and outside the synaptic cleft. Together, these information-rich tomographic maps
40 present a detailed molecular framework for the coordinated activity of synapses in the adult
41 mammalian brain.

INTRODUCTION

Glutamate is the major chemical neurotransmitter in the mammalian brain that mediates communication within neuronal circuits at specialized cell-cell junctions called synapses. The molecular composition of glutamatergic synapses is highly complex, reflecting the many different molecular machines required to subserve diverse synaptic functions, including learning and memory (Chua et al., 2010; Ebrahimi and Okabe, 2014; Frank et al., 2016; Nakahata and Yasuda, 2018). Indeed, more than a thousand different synaptic proteins have been identified in the mouse and human forebrain (Bayés et al., 2011; Roy et al., 2017). How this ensemble of macromolecules is structurally organized within adult mammalian brain synapses is currently unknown.

Cryo-electron microscopy (cryoEM) has the potential to reveal the native 3-dimensional molecular architecture of mammalian brain synapses but with the limitation that samples must be vitreous and less than ~300 nm thick. Although primary neurons grown on EM grids can overcome this constraint (Asano et al., 2015; Tao et al., 2018), the environment in which *in vitro* cultured cells grow differs markedly from tissues. Indeed, primary neurons *in vitro* appear unable to reach the molecular and functional maturity of neurons from the brain itself (Frank et al., 2016; Harris and Pettit, 2007). While brain synapses can be isolated by biochemical fractionation (Whittaker, 1959), these enrichment steps delay cryopreservation by at least an hour and involve non-physiological buffers that together cause deterioration of certain macromolecular structures. An example is the cytoskeleton, particularly microtubules, which rapidly depolymerize within a matter of 1-3 minutes if the provision of nucleotide triphosphates or cellular integrity becomes compromised (Mitchison, 1995; Pollard and Mooseker, 1981).

To minimize deterioration of tissue samples we developed an 'ultra-fresh' sample preparation workflow without fractionation by combining mouse genetic labelling of synapses (Zhu et al., 2018) with cryogenic correlated light and electron microscopy (cryoCLEM) and cryo-electron tomography (cryoET) (**Figure 1A**). Guided by the mouse genetic fluorescent label in our cryoCLEM workflow, we also determined the in-tissue 3D structure of synapses from vitreous cryo-sections of mouse cortex and hippocampus. These

71 ultra-fresh and in-tissue structural data indicate that the near-physiological molecular
72 architecture of glutamatergic synapses was highly variable in composition, copy number
73 and distribution of organelles and macromolecular assemblies. The molecular density of
74 protein complexes in the postsynaptic cytoplasm was variable and did not indicate a
75 conserved higher density of proteins at the postsynaptic membrane corresponding to a
76 postsynaptic density (PSD).

77 **RESULTS**

78 **CryoCLEM of adult brain glutamatergic synapses**

79 To determine the molecular architecture of adult forebrain excitatory synapses, we used
80 knockin mice, in which the gene encoding PSD95 was engineered to include an in-frame,
81 C-terminal fusion of the fluorescent tag EGFP (*Psd95*$^{GFP/GFP}$) (Broadhead et al., 2016;
82 Frank et al., 2016; Zhu et al., 2018). PSD95 is a membrane-associated cytoplasmic protein
83 that concentrates exclusively within mature glutamatergic synapses (Chen et al., 2000; El-
84 Husseini et al., 2000) and forms supercomplexes with ionotropic glutamate receptors that
85 reside in the postsynaptic membrane (Frank et al., 2016). Fresh *Psd95*$^{GFP/GFP}$ mouse
86 forebrains, encompassing cortex and hippocampus, were homogenized in ice-cold ACSF,
87 then immediately vitrified on EM grids. Sample preparation was completed within 2
88 minutes, the time taken to cull the mouse, dissect and homogenize the forebrain, and
89 plunge-freeze the sample on a blotted cryoEM grid (**Figure 1A**).

90 The GFP signal from *Psd95*$^{GFP/GFP}$ knockin mice pinpoints the location of mature
91 glutamatergic synapses without over-expression or any detectible effect on synapse
92 function (Broadhead et al., 2016). Thus, cryoEM grids were imaged on a cryogenic
93 fluorescence microscope (cryoFM) revealing PSD95-GFP puncta (**Figure 1A**), absent in
94 WT control samples (**Figure 1–figure supplement 1A**), which resembled those observed
95 by confocal fluorescent imaging of the brain (Zhu et al., 2018). Using a cryoCLEM
96 workflow, the same grids were then imaged by cryoEM and fluorescent PSD95-GFP
97 puncta were mapped onto the cryoEM image (**Figure 1B**). These cryoCLEM images
98 showed PSD95-GFP puncta that were invariably associated with membrane-bound

99 subcellular compartments (100 to 1,300 nm diameter) (**Figure 1B**).

100 To resolve the molecular architecture within PSD95-containing puncta, we acquired 93
101 PSD95-GFP cryoCLEM-guided cryo-electron tomographic tilt series from 5 adult mouse
102 forebrains. Aligned tilt series were reconstructed to produce 3-dimensional tomographic
103 maps as shown in **Figure 1C** and D (see also **Figure 1–table 1** and **Figure 1–video 1-7**
104 showing representative tomographic volumes of ultra-fresh synapses). As expected, all
105 GFP-positive membranes were attached to a neighbouring membrane, of which 78% were
106 closed compartments and enriched in synaptic vesicles that characterize the presynaptic
107 compartment. All but three of the presynaptic compartments (96%) contained docked
108 synaptic vesicles tethered 2-8 nm from presynaptic membrane (**Figure 1–figure**
109 **supplement 1B**). Thus, our PSD95-GFP cryoCLEM workflow enabled identification of
110 the pre- and post-synaptic membrane of glutamatergic synapses (hereon referred to as
111 PreSM and PoSM, respectively).

112 The high quality of the tomographic maps enabled assignment of cytoskeletal elements
113 within the synapse, including extensive networks of filamentous actin (F-actin). These
114 were identifiable with a diameter of 7 nm and apparent helical arrangement of subunits
115 (Hanson, 1967) in all PoSM compartments (Okamoto et al., 2007) (**Figure 1C-E** and
116 **Figure 1–figure supplement 1C**) and in 49±7% (mean ± SEM, n=5 mice) of PreSM
117 compartments (**Figure 1E** and **Figure 1–figure supplement 1D**). In PreSM that lacked an
118 apparent F-actin cytoskeletal network, we cannot exclude the possibility that actin is
119 present in monomeric form or very short actin filaments, which cannot be unambiguously
120 identified in our tomograms. Microtubules were identified (25 nm diameter) in 15±2% of
121 PreSM (**Figure 1C**, **D**, and **F**), but as expected were absent from the PoSM.
122 Notwithstanding the mechanical stress of detaching synaptic terminals to cryopreserve
123 whole synapses, this extensive actin and microtubular cytoskeleton corroborates the
124 maintenance of macromolecular structures near to their physiological context.

125 **Molecular crowding within the synapse**

126 We first assessed the overall architecture of macromolecules within the synapse by

127 measuring macromolecular crowding (Smith and Langmore, 1992) (see methods and
128 **Figure 1–figure supplement 2** detailing how molecular density was measured and how
129 confounding errors were avoided). Based on conventional EM experiments of fixed,
130 dehydrated, heavy-metal-stained tissue, glutamatergic synapses are marked by the presence
131 of a 30-50 nm layer of densely packed proteins opposite the active zone on the cytoplasmic
132 side of the PoSM, called the postsynaptic density (PSD) that defines every glutamatergic
133 synapse(Bourne and Harris, 2008; Gray, 1959; Sheng and Kim, 2011). However, within
134 fresh, adult brain synapse structures reported here this region of higher density at the
135 postsynaptic membrane was not a conserved feature of all PSD95-GFP-containing
136 glutamatergic synapses (**Figure 1g** and see also the central density profiles of each synapse
137 in **Figure 1–figure supplement 3**). The distribution of molecular densities was variable
138 with half the population of synapses showing a significant relative increase in molecular
139 density in proximal versus distal regions (5-30 nm versus 50-200 nm from the PoSM) of
140 cytoplasm in the postsynaptic compartment (**Figure 1H**). The remaining subpopulations of
141 synapses did not have a higher density or contained a significantly lower relative molecular
142 density at regions proximal to the PoSM (**Figure 1H,** two-tailed *t* test with Bonferroni
143 correction, $P< 0.05$, n=682 and 5673 voxels). These data suggest that a higher density of
144 proteins characteristic of the PSD is not a conserved feature with adult mouse brain
145 glutamatergic synapses (Tao et al., 2018).

146 To examine further molecular crowding within anatomically intact postsynaptic
147 compartments, fresh, acute brain tissues of 7 adult *Psd95*$^{GFP/GFP}$ mice were cryopreserved
148 by high-pressure freezing. Next, 70-150 nm thin, vitreous cryo-sections of the cortex and
149 hippocampus were collected by cryo-ultramicrotomy (**Figure 2A**) (Zuber et al., 2005).
150 Glutamatergic synapses were identified by cryoCLEM (**Figure 2B**) and cryo-electron
151 tomograms were collected revealing the native in-tissue 3D architecture of glutamatergic
152 synapses (**Figure 2C-D** and **Figure 2–figure supplement 1A** and **Figure 2-video 1-2**).
153 The PoSM was identified by cryoCLEM and the PreSM by the presence of numerous
154 synaptic vesicles. These in-tissue 3D tomographic maps also resolved individual
155 cytoskeletal elements, membrane proteins, and numerous other subcellular structures that
156 were consistent with those observed in ultra-fresh synapse cryoET data (**Figure 2–table**

157 **1**).

158 Molecular density profiles of in-tissue synapse cryoET data showed that the density of
159 proteins in the cytoplasm proximal to the PoSM relative to distal regions was highly
160 variable (**Figure 2E** and see also profiles of each synapse in **Figure 2–figure supplement**
161 **1B**). Less than half the population of synapses contained a significant relative increase in
162 molecular density in regions of the cytoplasm proximal to the PoSM (5-30 nm versus 50-
163 200 nm from the PoSM, **Figure 2F**). The remaining subpopulations of synapses lacked a
164 higher density or contained a significantly lower relative molecular density at regions
165 proximal to the PoSM (**Figure 2F,** two-tailed *t* test with Bonferroni correction, $P< 0.05$,
166 n=682 and 5673 voxels). No significant difference was observed comparing synapses from
167 the cortex versus hippocampus, as expected (Zhu et al., 2018). The variability of molecular
168 crowding in these near-physiological in-tissue synapses was consistent with the ultra-fresh
169 synapse tomograms, indicating that the presence of even a slight increase in cytoplasmic
170 molecular density that could correspond to a PSD was not a conserved feature of
171 glutamatergic synapses.

172 To rule out that the absence of a conserved postsynaptic protein dense region was caused
173 by the *Psd95*$^{GFP/GFP}$ knock-in mutation or the method of sample preparation, we performed
174 conventional EM of acute slice brain samples and ultra-fresh synapses, which showed a
175 PSD in samples from *Psd95*$^{GFP/GFP}$ comparable to those in wildtype mice (**Figure 2G-H**
176 and **Figure 2–figure supplement 2A-B**). This confirmed that the appearance of the high
177 local protein density that defines the PSD is a consequence of conventional EM sample
178 preparation methods.

179 **Synaptic organelles**

180 To assess the molecular diversity of adult forebrain excitatory synapse architecture we next
181 catalogued the identifiable macromolecular and organelle constituents in ultra-fresh
182 synapses (**Figure 1–table 1**). At least one membrane-bound organelle was present in
183 61±4% of PoSM compartments and, excluding synaptic vesicles, in 77±2% of PreSM
184 compartments (**Figure 3–figure supplement 1A**). Based on previous characterizations by

185 conventional EM studies (Cooney et al., 2002) most membrane-bound organelles were
186 readily separable into three structural classes (**Figure 3–figure supplement 1B** and **Figure**
187 **1–table 1**, see methods): 1) A network of flat, tubular membrane compartments that twisted
188 and projected deep toward the adhered synaptic membrane (**Figure 3A** and **Figure 3–**
189 **figure supplement 1B-C**). 2) Large spheroidal membrane compartments (>60 nm
190 diameter) that were situated 72-500 nm away from the cleft (**Figure 3A** and **Figure 3–**
191 **figure supplement 1B**, **D**). 3) Multivesicular bodies that were positioned throughout the
192 PreSM and PoSM (78-360 nm away from the cleft, **Figure 3B** and **Figure 3–figure**
193 **supplement 1B**, **E**). A fourth category of membranous compartments found in our data did
194 not match any of the structures previously reported and can be characterized as polyhedral
195 vesicles with flat surfaces and joined by protein-coated membrane edges and vertices (90°
196 to 35° internal angle, **Figure 3C** and **Figure 3–figure supplement 1F**).

197 Mitochondria were also readily identified, most abundantly in the presynaptic compartment
198 (44±5% of PreSM) and only once in close proximity to the postsynaptic compartment
199 (**Figure 3–figure supplement 1G**). A striking feature of all presynaptic mitochondria was
200 the presence of amorphous dense aggregates within the mitochondrial matrix (**Figure 3–**
201 **figure supplement 1H**). Similar aggregates have been identified as solid deposits of
202 calcium phosphate (Wolf et al., 2017) and are apparent in cultured neurons (Tao et al.,
203 2018). To exclude the possibility that mitochondrial aggregates arose by excitation during
204 sample preparation we collected tomograms of ultra-fresh synapses prepared in ACSF that
205 lacked divalent cations, including calcium (**Figure 3–figure supplement 1I**). These data
206 showed synapses with mitochondrial aggregates in the absence of exogenous calcium,
207 suggesting they do not arise during sample preparation. Thus, mitochondrial granular
208 aggregates likely represent a physiologically normal feature of the mammalian brain, which
209 is in keeping with the role of synaptic mitochondria as a reservoir of cellular calcium ions
210 (Billups and Forsythe, 2002). Overall, the variable protein composition and type of
211 intracellular organelles indicate distinct synapse subtypes or states within the mammalian
212 forebrain.

213 **Synaptic shape and remodeling**

214 Further diversity of synaptic architectures was evident in the size, shape and mode of
215 connectivity of the PreSM to the PoSM (Zhu et al., 2018). To assess these structural
216 variables, PSD95-GFP-containing PoSMs and apposing PreSMs were semi-automatically
217 segmented (see methods). This revealed synapses with multiple different topologies,
218 including with single, double, and divergent (1 PreSM: 2 PoSM) synaptic contacts (**Figure**
219 **3D**, *top*, *middle* and *bottom*, respectively and **Figure 1–table 1**). These were consistent
220 with the known diversity of cellular connectivity mediated by glutamatergic synapses
221 (Harris and Weinberg, 2012). The volume of the PoSM compartment in our dataset ranged
222 from $3x10^6$ to $79x10^6$ nm^3. In keeping with the known diversity of PSD95-containing
223 synapses (Zhu et al., 2018) and *in vivo* fluorescence imaging experiments (Melander et al.,
224 2021), PoSM size was not correlated with the amount of PSD95-GFP detected by
225 cryoCLEM (P=0.7, Pearson's r=0.06, **Figure 3E**)(Melander et al., 2021). However, PoSM
226 size was correlated with the number of actin cytoskeletal filaments (P<0.0001, Pearson's
227 r=0.83, **Figure 3F**), which is in line with the apparent non-uniform distribution of F-actin
228 in distinct sub-cellular compartments (**Figure 1E**) and the role of F-actin in regulating
229 postsynaptic geometry and structural plasticity (Okamoto et al., 2007) .

230 The variation in size, shape and molecular composition of synaptic membranes is thought
231 to arise by membrane remodeling, including exo- and endocytosis. In 32±6% synapses we
232 identified pit-like, hemifusion or hemifission structures in the membrane (**Figure 3–figure**
233 **supplement 1J**) that likely indicate intermediates of membrane remodeling trapped within
234 the sample at the moment of freezing (**Figure 1–table 1**). Significantly more remodeling
235 intermediates were identified in the PreSM compared to PoSM compartments (**Figure 3G**,
236 Paired two-tailed *t* test, P=0.021, n=5 mice), which is consistent with the expected high
237 frequency of membrane dynamics associated with synaptic vesicle recycling in this
238 compartment (Kononenko and Haucke, 2015).

239 In a subset of tomograms (21±11%, Fig 3h) a clathrin coat was unambiguously identified
240 by the triskelion-forming pentagonal and hexagonal openings (Kanaseki and Kadota, 1969;
241 Kravčenko et al., 2024) evident in the raw tomographic maps (**Figure 1–table 1**). In the
242 pre-synaptic compartment, clathrin surrounded synaptic vesicles (**Figure 3I**) and budding
243 vesicles on internal membrane compartments (**Figure 3J**), which is in agreement with

244 previous time-resolved EM experiments (Watanabe et al., 2014). In the postsynaptic
245 compartment, a clathrin-coated pit formed directly on the cleft, suggesting membrane and
246 cargo can be removed without prior lateral diffusion out of the synapse (**Figure 3K**). Thus,
247 the distribution of these distinct intermediates suggests that membrane remodeling occurs
248 at particular sub-compartments of the synapse (Borges-Merjane et al., 2020; Imig et al.,
249 2020; Watanabe et al., 2014).

250 **Synaptic cleft and ionotropic glutamate receptors**

251 Geometric properties of each synapse are thought to be critical for determining synaptic
252 strength, including synaptic cleft height (Cathala et al., 2005; Rusakov et al., 2011),
253 measured as the shortest distance between PreSM and PoSM. To quantify this variable in
254 our dataset we computationally determined the 3D coordinates of the cleft within each
255 synapse (**Figure 4–figure supplement 1A** and see methods). The PreSM to PoSM
256 distances across the cleft indicated an average cleft height of 33 nm (**Figure 4A**). These
257 values differ from average cleft heights of ~20 nm determined in non-native conditions by
258 conventional EM (Peters et al., 1970) but are consistent with super-resolution light
259 microscopy imaging (Tønnesen et al., 2018). Interestingly, the average cleft height of each
260 synapse in our dataset varied (ranging from 27 to 37 nm)[8]. A similar range of cleft distances
261 were observed in in-tissue synapse tomograms (**Figure 2C** and **Figure 2–figure**
262 **supplement 1**), suggesting that the cleft dimensions were largely unaffected by the ultra-
263 fresh sample preparation. A subset of 'ultra-fresh' synapses maintained a very broad or
264 bimodal distribution of cleft heights (**Figure 4–figure supplement 1B**). Inspection of
265 synapses with a broad or bimodal distribution revealed closely apposed and remotely
266 spaced subsynaptic regions of the cleft, containing transsynaptic complexes with varying
267 dimensions that complemented the cleft height of the subregion (**Figure 4–figure**
268 **supplement 1C-D**). Closely opposed synaptic subregions were found both near the edge
269 and the middle of the cleft, consistent with the notion that cleft height is locally regulated.
270 Thus, these data suggest the synaptic cleft as a highly plastic interface, in which cleft
271 dimensions are dictated by the variable molecular composition of transsynaptic adhesion
272 complexes (Missler et al., 2012).

273 The number, concentration, and distribution of ionotropic glutamate receptors anchored at
274 the postsynaptic membrane by PSD95 is a central determinant of synaptic output (Béïque
275 et al., 2006; Cathala et al., 2005; Kerr and Blanpied, 2012; Migaud et al., 1998; Rusakov
276 et al., 2011; Tang et al., 2016). Putative ionotropic glutamate receptors were readily
277 identified in 95±2% of PoSMs. These resembled the side (**Figure 4B** *left*) and top views
278 (**Figure 4B** *right*) of ionotropic glutamate receptor atomic models (Hansen et al., 2021;
279 Regan et al., 2015; Zhu and Gouaux, 2017). To confirm the identity of these proteins, we
280 manually picked 2,522 receptors and extracted sub-volumes at those positions. We then
281 applied subtomogram averaging procedures (see methods), which gave a 25 Å resolution
282 'Y' shaped cryoEM density map extending 14 nm from the PoSM (**Figure 4–figure**
283 **supplement 2A**). The density shows a 2-fold symmetric structure containing two layers of
284 globular domains in positions proximal and distal to the PoSM (**Figure 4C**) as expected
285 for the structure of an ionotropic glutamate receptor. Consequently, the atomic structure
286 of the AMPA receptor was well accommodated by the density, which supports the
287 identification of these ion channels within our synapse tomogram dataset (**Figure 4C**).

288 Next, to analyse the 3D configuration of populations of ionotropic glutamate receptors, we
289 used these coordinates to quantify receptor clusters (see methods). Clusters were identified
290 in 78% of synapses with an average of 2 clusters per synapse (**Figure 4D**), which were
291 composed of up to 60 ionotropic glutamate receptors (average 10 receptors per cluster)
292 (**Figure 4E**). These subsynaptic regions with higher concentrations of ionotropic glutamate
293 receptors were reminiscent of receptor 'nanodomains' detected by super-resolution
294 microscopy (Broadhead et al., 2016; Dani et al., 2010; MacGillavry et al., 2013; Nair et al.,
295 2013; Tang et al., 2016).

296 The position of ionotropic receptor clusters in synaptic and extra-synaptic sites, particularly
297 the most abundant AMPA receptor subtype, is expected to impact synaptic strength and
298 play an important role in synaptic plasticity (Park, 2018). We therefore analyzed the
299 distribution of clusters in the context of the overall synapse architecture, which revealed
300 that 60% of synapses maintained multiple large clusters of ionotropic glutamate receptors
301 completely or partly outside of the cleft (**Figure 4D-F**). The apparent detection of
302 perisynaptic populations of glutamate receptors resemble the distributions observed by

303 previous freeze-fracture immunogold EM (Masugi-Tokita and Shigemoto, 2007) and
304 super-resolution light microscopy (Nair et al., 2013). The close proximity of perisynaptic
305 clusters to the cleft is consistent with the functional necessity of a non-cleft population of
306 ionotropic glutamate receptors that are recruited into the cleft during the early phase of
307 long-term potentiation (Penn et al., 2017). Interestingly, the cytoplasmic C-termini of
308 ionotropic receptor clusters both inside and outside of the cleft were situated adjacent to
309 an elaborate and heterogeneous membrane- and actin-associated machinery (**Figure 4–**
310 **figure supplement 2B**), possibly indicating that a structural mechanism contributes to the
311 positioning of receptors both inside and outside the synaptic cleft.

312 **Discussion**

313 Here we determined the near-physiological 3D molecular architecture of glutamatergic
314 synapses in the adult mammalian brain. In both ultra fresh and anatomically intact in-tissue
315 cryoET datasets, a conserved relatively higher molecular density consistent with a PSD
316 was absent. Instead, we observed subtle variations in molecular crowding within our
317 cryoET dataset. The PSD has been a defining structure of glutamatergic synapses and has
318 been most frequently observed by conventional EM (Bourne and Harris, 2008; Sheng and
319 Kim, 2011), including when using more recent methods that involve freeze-substitution
320 into organic solvents, followed by heavy-metal staining (Chen et al., 2008). We addressed
321 the hypothesis that the occurrence of a PSD might be related to sample preparation and
322 staining techniques of conventional EM by preparing the same mouse brain samples for
323 conventional EM and were indeed able to reproduce the conserved occurrence of a PSD.
324 We therefore suggest that the appearance of a PSD in room temperature EM experiments
325 could arise during sample preparation. Preferential heavy-metal staining, crosslinking of
326 interacting proteins by fixatives, or extraction of cytoplasmic proteins that are not directly
327 or indirectly associated with the postsynaptic membrane could alter the apparent local
328 distribution or relative density of proteins in tissue samples prepared by resin-embedding
329 and freeze-substitution EM methods.

330 CryoEM of *in vitro* cultured organotypic slice cultures that first demonstrated the use of
331 high-pressure freezing neuronal tissue samples, revealed synapses with various pre- and

332 post- and trans-synaptic regions containing relatively higher densities (Zuber et al., 2005),
333 albeit these data also lacked a label to confirm which synapses in the sample were
334 glutamatergic.

335 Pioneering cryoET work of synapses purified from brain (synaptosomes) suggested a
336 slightly higher relative molecular density juxtaposed to the postsynaptic membrane
337 (Fernández-Busnadiego et al., 2010). However, interpretation of synaptosome
338 architectures may be compromised by lengthy sample preparation in non-physiological
339 solutions that may cause a loss of cytoplasm and the native molecular architecture. Indeed,
340 the marked absence of microtubules in synaptosomes is indicative of sample deterioration.
341 It was also previously challenging to identify glutamatergic synapses definitively.
342 Consequently, synaptosomes that lacked an apparent postsynaptic thickening were actively
343 excluded from data collection (Martinez-Sanchez et al., 2021).

344 More recent cryoCLEM and cryoET studies of primary neuronal cell cultures identified
345 glutamatergic synapses with some but not all showing a subtly higher concentration of
346 macromolecules juxtaposed to the PoSM relative to distal regions deep within the
347 postsynaptic compartment (Tao et al., 2018). These data were consistent with ultra-fresh
348 synapse tomograms from adult brain, including the preservation of microtubules in the
349 presynaptic compartment. A greater fraction of ultra-fresh adult synapses resembled the
350 minority of primary neuronal synapses that lacked a relative increase in molecular
351 crowding at the PoSM. In anatomically intact brain slice preparations that were nearer to
352 physiological state of adult brain, even fewer instances of synapses were observed with a
353 relative increase in molecular crowding of the cytoplasm at the PoSM. We suggest that
354 these subtle differences of molecular crowding are likely a consequence of synapse
355 heterogeneity (Zhu et al., 2018) or the source, in vitro cell culture versus adult brain, of
356 central synapses. More broadly these cryoET data were consistent in suggesting that a
357 relatively higher concentration of proteins juxtaposed to the PoSM is neither conserved nor
358 a defining feature of glutamatergic synapses.

359 The synaptic architectures reported here were nevertheless consistent with the existence of
360 specialized protein nanodomains of particular synaptic constituents detected by

361 fluorescence labeling, including of PSD95 (Broadhead et al., 2016; Dani et al., 2010;
362 MacGillavry et al., 2013; Nair et al., 2013; Tang et al., 2016). Indeed, clusters of ionotropic
363 glutamate receptors that are anchored via interactions with PSD95 (Dani et al., 2010;
364 MacGillavry et al., 2013; Nair et al., 2013; Tang et al., 2016) were a salient feature in
365 tomographic maps of adult brain synapses.

366 We also evaluated the dimensions of the synaptic cleft, which is expected to affect synaptic
367 strength (Rusakov et al., 2011). Cleft height was highly variable and on average 65%
368 greater than that observed by conventional EM, which is also likely explained by the harsh
369 treatments and the well-characterised shrinkage associated with chemical fixation of
370 tissues in conventional EM. More broadly, these comparisons highlight the advantages of
371 combining recent advances in cryoET (Turk and Baumeister, 2020) with genetic knockin
372 labelling to determine the molecular architecture of fresh tissues.

373 Notwithstanding the absence of a conserved PSD, the arrangement of prominent
374 constituents, including branched F-actin networks, organelles, ionotropic glutamate
375 receptors and transsynaptic adhesion complexes, appeared to define the architecture of each
376 glutamatergic synapse. Overall, the apparent variability of molecular and membrane
377 architectures, from one synapse tomogram to the next, is in keeping with the enormous
378 diversity of glutamatergic synapse types in the mammalian brain (Zhu et al., 2018). Since
379 submission of our manuscript, several reports of synapse cryoET from within cultured
380 primary neurons(Held et al., 2024a, 2024b) and mouse brain(Glynn et al., 2024; Matsui et
381 al., 2024) were prepared by cryoFIB-milling. These new datasets are largely consistent
382 with the data reported here. CryoFIB-milling has the advantage of overcoming the local
383 knife damage caused by cryo-sectioning but introduces amorphization across the whole
384 sample that diminishes the information content (Al-Amoudi et al., 2005; Lovatt et al., 2022;
385 Lucas and Grigorieff, 2023). We have recently shown that cryoET data is capable of
386 revealing subnanometer resolution in-tissue protein structure from vitreous cryo-sections
387 (Gilbert et al., 2024) and near-atomic structure determination from vitreous cryo-sections
388 has recently been demonstrated (Elferich et al., 2025). A future challenge will be to
389 decipher how synaptic structural variability across the dendritic tree, different brain regions
390 and neuronal subtypes determine specific functions within the mammalian brain.

391 **References**

392 Al-Amoudi A, Studer D, Dubochet J. 2005. Cutting artefacts and cutting process in
393 vitreous sections for cryo-electron microscopy. *J Struct Biol* **150**:109–121.
394 doi:10.1016/j.jsb.2005.01.003

395 Asano S, Fukuda Y, Beck F, Aufderheide A, Förster F, Danev R, Baumeister W. 2015. A
396 molecular census of 26*S* proteasomes in intact neurons. *Science* **347**:439–442.
397 doi:10.1126/science.1261197

398 Bayés À, Lagemaat LN van de, Collins MO, Croning MDR, Whittle IR, Choudhary JS,
399 Grant SGN. 2011. Characterization of the proteome, diseases and evolution of the
400 human postsynaptic density. *Nat Neurosci* **14**:19–21. doi:10.1038/nn.2719

401 Béïque J-C, Lin D-T, Kang M-G, Aizawa H, Takamiya K, Huganir RL. 2006. Synapse-
402 specific regulation of AMPA receptor function by PSD-95. *Proc National Acad Sci*
403 **103**:19535–19540. doi:10.1073/pnas.0608492103

404 Billups B, Forsythe ID. 2002. Presynaptic Mitochondrial Calcium Sequestration
405 Influences Transmission at Mammalian Central Synapses. *J Neurosci* **22**:5840–5847.
406 doi:10.1523/jneurosci.22-14-05840.2002

407 Borges-Merjane C, Kim O, Jonas P. 2020. Functional Electron Microscopy, "Flash and
408 Freeze," of Identified Cortical Synapses in Acute Brain Slices. *Neuron* **105**:992-
409 1006.e6. doi:10.1016/j.neuron.2019.12.022

410 Bourne JN, Harris KM. 2008. Balancing Structure and Function at Hippocampal
411 Dendritic Spines. *Annu Rev Neurosci* **31**:47–67.
412 doi:10.1146/annurev.neuro.31.060407.125646

413 Broadhead MJ, Horrocks MH, Zhu F, Muresan L, Benavides-Piccione R, DeFelipe J,
414 Fricker D, Kopanitsa MV, Duncan RR, Klenerman D, Komiyama NH, Lee SF, Grant
415 SGN. 2016. PSD95 nanoclusters are postsynaptic building blocks in hippocampus
416 circuits. *Sci Rep* **6**:24626. doi:10.1038/srep24626

417 Castaño-Díez D, Kudryashev M, Stahlberg H. 2017. Dynamo Catalogue: Geometrical
418 tools and data management for particle picking in subtomogram averaging of cryo-
419 electron tomograms. *J Struct Biol* **197**:135–144. doi:10.1016/j.jsb.2016.06.005

420 Cathala L, Holderith NB, Nusser Z, DiGregorio DA, Cull-Candy SG. 2005. Changes in
421 synaptic structure underlie the developmental speeding of AMPA receptor–mediated
422 EPSCs. *Nat Neurosci* **8**:1310–1318. doi:10.1038/nn1534

423 Chen L, Chetkovich DM, Petralia RS, Sweeney NT, Kawasaki Y, Wenthold RJ, Bredt
424 DS, Nicoll RA. 2000. Stargazin regulates synaptic targeting of AMPA receptors by
425 two distinct mechanisms. *Nature* **408**:936–943. doi:10.1038/35050030

426 Chen S, McMullan G, Faruqi AR, Murshudov GN, Short JM, Scheres SHW, Henderson
427 R. 2013. High-resolution noise substitution to measure overfitting and validate
428 resolution in 3D structure determination by single particle electron cryomicroscopy.
429 *Ultramicroscopy* **135**:24–35. doi:10.1016/j.ultramic.2013.06.004

430 Chen X, Winters C, Azzam R, Li X, Galbraith JA, Leapman RD, Reese TS. 2008.
431 Organization of the core structure of the postsynaptic density. *Proc Natl Acad Sci*
432 **105**:4453–4458. doi:10.1073/pnas.0800897105

433 Chua JJE, Kindler S, Boyken J, Jahn R. 2010. The architecture of an excitatory synapse. *J*
434 *Cell Sci* **123**:819–823. doi:10.1242/jcs.052696

435 Cooney JR, Hurlburt JL, Selig DK, Harris KM, Fiala JC. 2002. Endosomal
436 Compartments Serve Multiple Hippocampal Dendritic Spines from a Widespread
437 Rather Than a Local Store of Recycling Membrane. *J Neurosci* **22**:2215–2224.
438 doi:10.1523/jneurosci.22-06-02215.2002

439 Dani A, Huang B, Bergan J, Dulac C, Zhuang X. 2010. Superresolution Imaging of
440 Chemical Synapses in the Brain. *Neuron* **68**:843–856.
441 doi:10.1016/j.neuron.2010.11.021

442 Ebrahimi S, Okabe S. 2014. Structural dynamics of dendritic spines: Molecular
443 composition, geometry and functional regulation. *Biochim Biophys Acta (BBA) -*
444 *Biomembr* **1838**:2391–2398. doi:10.1016/j.bbamem.2014.06.002

445 Elferich J, Kaminek M, Kong L, Odriozola A, Kukulski W, Zuber B, Grigorieff N. 2025.
446 In-Situ High-Resolution Cryo-EM Reconstructions from CEMOVIS. *bioRxiv*
447 2025.03.29.646093. doi:10.1101/2025.03.29.646093

448 El-Husseini AE-D, Schnell E, Chetkovich DM, Nicoll RA, Bredt DS. 2000. PSD-95
449 Involvement in Maturation of Excitatory Synapses. *Science* **290**:1364–1368.
450 doi:10.1126/science.290.5495.1364

451 Fäßler F, Dimchev G, Hodirnau V-V, Wan W, Schur FKM. 2020. Cryo-electron
452 tomography structure of Arp2/3 complex in cells reveals new insights into the branch
453 junction. *Nat Commun* **11**:6437. doi:10.1038/s41467-020-20286-x

454 Fernández-Busnadiego R, Zuber B, Maurer UE, Cyrklaff M, Baumeister W, Lučić V.
455 2010. Quantitative analysis of the native presynaptic cytomatrix by cryoelectron
456 tomography. *J Cell Biol* **188**:145–156. doi:10.1083/jcb.200908082

457 Förster F, Medalia O, Zauberman N, Baumeister W, Fass D. 2005. Retrovirus envelope
458 protein complex structure in situ studied by cryo-electron tomography. *Proc Natl Acad*
459 *Sci* **102**:4729–4734. doi:10.1073/pnas.0409178102

460 Frank RAW, Komiyama NH, Ryan TJ, Zhu F, O'Dell TJ, Grant SGN. 2016. NMDA
461 receptors are selectively partitioned into complexes and supercomplexes during
462 synapse maturation. *Nat Commun* **7**:11264. doi:10.1038/ncomms11264

463 Fukuda Y, Laugks U, Lučić V, Baumeister W, Danev R. 2015. Electron cryotomography
464 of vitrified cells with a Volta phase plate. *J Struct Biol* **190**:143–154.
465 doi:10.1016/j.jsb.2015.03.004

466 Gilbert MAG, Fatima N, Jenkins J, O'Sullivan TJ, Schertel A, Halfon Y, Wilkinson M,
467 Morrema THJ, Geibel M, Read RJ, Ranson NA, Radford SE, Hoozemans JJM, Frank
468 RAW. 2024. CryoET of β-amyloid and tau within postmortem Alzheimer's disease
469 brain. *Nature* **631**:913–919. doi:10.1038/s41586-024-07680-x

470 Glynn C, Smith JLR, Case M, Csöndör R, Katsini A, Sanita ME, Glen TS, Pennington A,
471 Grange M. 2024. Charting the molecular landscape of neuronal organisation within
472 the hippocampus using cryo electron tomography. *bioRxiv* 2024.10.14.617844.
473 doi:10.1101/2024.10.14.617844

474 Gray EG. 1959. Axo-somatic and axo-dendritic synapses of the cerebral cortex: an
475 electron microscope study. *J Anat* **93**:420–33. doi:10.1111/j.1415-5195.1959.00420.x

476 Hagen WJH, Wan W, Briggs JAG. 2017. Implementation of a cryo-electron tomography
477 tilt-scheme optimized for high resolution subtomogram averaging. *J Struct Biol*
478 **197**:191–198. doi:10.1016/j.jsb.2016.06.007

479 Hansen KB, Wollmuth LP, Bowie D, Furukawa H, Menniti FS, Sobolevsky AI, Swanson
480 GT, Swanger SA, Greger IH, Nakagawa T, McBain CJ, Jayaraman V, Low C-M,
481 Dell'Acqua ML, Diamond JS, Camp CR, Perszyk RE, Yuan H, Traynelis SF. 2021.
482 Structure, Function, and Pharmacology of Glutamate Receptor Ion Channels.
483 *Pharmacol Rev* **73**:298–487. doi:10.1124/pharmrev.120.000131

484 Hanson J. 1967. Axial Period of Actin Filaments. *Nature* **213**:353–356.
485 doi:10.1038/213353a0

486 Harris AZ, Pettit DL. 2007. Extrasynaptic and synaptic NMDA receptors form stable and
487 uniform pools in rat hippocampal slices. *J Physiol* **584**:509–519.
488 doi:10.1113/jphysiol.2007.137679

489 Harris KM, Weinberg RJ. 2012. Ultrastructure of Synapses in the Mammalian Brain.
490 *Cold Spring Harb Perspect Biol* **4**:a005587. doi:10.1101/cshperspect.a005587

491 Held RG, Liang J, Brunger AT. 2024a. Nanoscale architecture of synaptic vesicles and
492 scaffolding complexes revealed by cryo-electron tomography. *Proc Natl Acad Sci*
493 **121**:e2403136121. doi:10.1073/pnas.2403136121

494 Held RG, Liang J, Esquivies L, Khan YA, Wang C, Azubel M, Brunger AT. 2024b. In-
495 Situ Structure and Topography of AMPA Receptor Scaffolding Complexes Visualized
496 by CryoET. *bioRxiv* 2024.10.19.619226. doi:10.1101/2024.10.19.619226

497 Imig C, López-Murcia FJ, Maus L, García-Plaza IH, Mortensen LS, Schwark M,
498 Schwarze V, Angibaud J, Nägerl UV, Taschenberger H, Brose N, Cooper BH. 2020.
499 Ultrastructural Imaging of Activity-Dependent Synaptic Membrane-Trafficking
500 Events in Cultured Brain Slices. *Neuron* **108**:843-860.e8.
501 doi:10.1016/j.neuron.2020.09.004

502 Kanaseki T, Kadota K. 1969. The "Vesicle in a Basket": A Morphological Study of the
503 Coated Vesicle Isolated from the Nerve Endings of the Guinea Pig Brain, with Special
504 Reference to the Mechanism of Membrane Movements. *J Cell Biol* **42**:202–220.
505 doi:10.1083/jcb.42.1.202

506 Kerr JM, Blanpied TA. 2012. Subsynaptic AMPA Receptor Distribution Is Acutely
507 Regulated by Actin-Driven Reorganization of the Postsynaptic Density. *J Neurosci*
508 **32**:658–673. doi:10.1523/jneurosci.2927-11.2012

509 Kononenko NL, Haucke V. 2015. Molecular Mechanisms of Presynaptic Membrane
510 Retrieval and Synaptic Vesicle Reformation. *Neuron* **85**:484–496.
511 doi:10.1016/j.neuron.2014.12.016

512 Kravčenko U, Ruwolt M, Kroll J, Yushkevich A, Zenkner M, Ruta J, Lotfy R, Wanker
513 EE, Rosenmund C, Liu F, Kudryashev M. 2024. Molecular architecture of synaptic
514 vesicles. *Proc Natl Acad Sci* **121**:e2407375121. doi:10.1073/pnas.2407375121

515 Kremer JR, Mastronarde DN, McIntosh JR. 1996. Computer Visualization of Three-
516 Dimensional Image Data Using IMOD. *J Struct Biol* **116**:71–76.
517 doi:10.1006/jsbi.1996.0013

518 Kukulski W, Schorb M, Welsch S, Picco A, Kaksonen M, Briggs JAG. 2011. Correlated
519 fluorescence and 3D electron microscopy with high sensitivity and spatial precision. *J*
520 *Cell Biol* **192**:111–119. doi:10.1083/jcb.201009037

521 Lovatt M, Leistner C, Frank RAW. 2022. Bridging length scales from molecules to the
522 whole organism by cryoCLEM and cryoET. *Faraday Discuss* **240**:114–126.
523 doi:10.1039/d2fd00081d

524 Lowenthal MS, Markey SP, Dosemeci A. 2015. Quantitative Mass Spectrometry
525 Measurements Reveal Stoichiometry of Principal Postsynaptic Density Proteins. *J*
526 *Proteome Res* **14**:2528–2538. doi:10.1021/acs.jproteome.5b00109

527 Lucas BA, Grigorieff N. 2023. Quantification of gallium cryo-FIB milling damage in
528 biological lamellae. *Proc Natl Acad Sci* **120**:e2301852120.
529 doi:10.1073/pnas.2301852120

530 MacGillavry HD, Song Y, Raghavachari S, Blanpied TA. 2013. Nanoscale Scaffolding
531 Domains within the Postsynaptic Density Concentrate Synaptic AMPA Receptors.
532 *Neuron* **78**:615–622. doi:10.1016/j.neuron.2013.03.009

533 Martinez-Sanchez A, Laugks U, Kochovski Z, Papantoniou C, Zinzula L, Baumeister W,
534 Lučić V. 2021. Trans-synaptic assemblies link synaptic vesicles and neuroreceptors.
535 *Sci Adv* **7**:eabe6204. doi:10.1126/sciadv.abe6204

536 Mastronarde DN. 2005. Automated electron microscope tomography using robust
537 prediction of specimen movements. *J Struct Biol* **152**:36–51.
538 doi:10.1016/j.jsb.2005.07.007

539 Masugi-Tokita M, Shigemoto R. 2007. High-resolution quantitative visualization of
540 glutamate and GABA receptors at central synapses. *Curr Opin Neurobiol* **17**:387–393.
541 doi:10.1016/j.conb.2007.04.012

542 Matsui A, Spangler C, Elferich J, Shiozaki M, Jean N, Zhao X, Qin M, Zhong H, Yu Z,
543 Gouaux E. 2024. Cryo-electron tomographic investigation of native hippocampal
544 glutamatergic synapses. *eLife* **13**:RP98458. doi:10.7554/elife.98458

545 Melander JB, Nayebi A, Jongbloets BC, Fortin DA, Qin M, Ganguli S, Mao T, Zhong H.
546 2021. Distinct in vivo dynamics of excitatory synapses onto cortical pyramidal
547 neurons and parvalbumin-positive interneurons. *Cell Reports* **37**:109972.
548 doi:10.1016/j.celrep.2021.109972

549 Migaud M, Charlesworth P, Dempster M, Webster LC, Watabe AM, Makhinson M, He
550 Y, Ramsay MF, Morris RGM, Morrison JH, O'Dell TJ, Grant SGN. 1998. Enhanced
551 long-term potentiation and impaired learning in mice with mutant postsynaptic
552 density-95 protein. *Nature* **396**:433–439. doi:10.1038/24790

553 Missler M, Südhof TC, Biederer T. 2012. Synaptic Cell Adhesion. *Cold Spring Harb*
554 *Perspect Biol* **4**:a005694. doi:10.1101/cshperspect.a005694

555 Mitchison TJ. 1995. Evolution of a dynamic cytoskeleton. *Philos Trans R Soc Lond Ser*
556 *B: Biol Sci* **349**:299–304. doi:10.1098/rstb.1995.0117

557 Nair D, Hosy E, Petersen JD, Constals A, Giannone G, Choquet D, Sibarita J-B. 2013.
558 Super-Resolution Imaging Reveals That AMPA Receptors Inside Synapses Are
559 Dynamically Organized in Nanodomains Regulated by PSD95. *J Neurosci* **33**:13204–
560 13224. doi:10.1523/jneurosci.2381-12.2013

561 Nakahata Y, Yasuda R. 2018. Plasticity of Spine Structure: Local Signaling, Translation
562 and Cytoskeletal Reorganization. *Front Synaptic Neurosci* **10**:29.
563 doi:10.3389/fnsyn.2018.00029

564 Nickell S, Förster F, Linaroudis A, Net WD, Beck F, Hegerl R, Baumeister W, Plitzko
565 JM. 2005. TOM software toolbox: acquisition and analysis for electron tomography. *J*
566 *Struct Biol* **149**:227–234. doi:10.1016/j.jsb.2004.10.006

567 Okamoto K-I, Narayanan R, Lee SH, Murata K, Hayashi Y. 2007. The role of CaMKII as
568 an F-actin-bundling protein crucial for maintenance of dendritic spine structure. *Proc*
569 *Natl Acad Sci* **104**:6418–6423. doi:10.1073/pnas.0701656104

570 Park M. 2018. AMPA Receptor Trafficking for Postsynaptic Potentiation. *Front Cell*
571 *Neurosci* **12**:361. doi:10.3389/fncel.2018.00361

572 Penn AC, Zhang CL, Georges F, Royer L, Breillat C, Hosy E, Petersen JD, Humeau Y,
573 Choquet D. 2017. Hippocampal LTP and contextual learning require surface diffusion
574 of AMPA receptors. *Nature* **549**:384–388. doi:10.1038/nature23658

575 Peters A, Palay SL, Webster HF. 1970. The fine structure of the nervous system: the cells
576 and their processes.

577 Pettersen EF, Goddard TD, Huang CC, Couch GS, Greenblatt DM, Meng EC, Ferrin TE.
578 2004. UCSF Chimera—A visualization system for exploratory research and analysis. *J*
579 *Comput Chem* **25**:1605–1612. doi:10.1002/jcc.20084

580 Pizarro-Cerdá J, Chorev DS, Geiger B, Cossart P. 2017. The Diverse Family of Arp2/3
581 Complexes. *Trends Cell Biol* **27**:93–100. doi:10.1016/j.tcb.2016.08.001

582 Pollard TD, Mooseker MS. 1981. Direct measurement of actin polymerization rate
583 constants by electron microscopy of actin filaments nucleated by isolated microvillus
584 cores. *J cell Biol* **88**:654–659. doi:10.1083/jcb.88.3.654

585 Regan MC, Romero-Hernandez A, Furukawa H. 2015. A structural biology perspective
586 on NMDA receptor pharmacology and function. *Curr Opin Struc Biol* **33**:68–75.
587 doi:10.1016/j.sbi.2015.07.012

588 Roy M, Sorokina O, Skene N, Simonnet C, Mazzo F, Zwart R, Sher E, Smith C,
589 Armstrong JD, Grant SGN. 2017. Proteomic analysis of postsynaptic proteins in
590 regions of the human neocortex. *Nat Neurosci* **21**:1–9. doi:10.1038/s41593-017-0025-
591 9

592 Rusakov DA, Savtchenko LP, Zheng K, Henley JM. 2011. Shaping the synaptic signal:
593 molecular mobility inside and outside the cleft. *Trends Neurosci* **34**:359–369.
594 doi:10.1016/j.tins.2011.03.002

595 Schorb M, Briggs JAG. 2014. Correlated cryo-fluorescence and cryo-electron
596 microscopy with high spatial precision and improved sensitivity. *Ultramicroscopy*
597 **143**:24–32. doi:10.1016/j.ultramic.2013.10.015

598 Sheng M, Kim E. 2011. The Postsynaptic Organization of Synapses. *Cold Spring Harb*
599 *Perspect Biol* **3**:a005678. doi:10.1101/cshperspect.a005678

600 Smith MF, Langmore JP. 1992. Quantitation of molecular densities by cryo-electron
601 microscopy Determination of the radial density distribution of tobacco mosaic virus. *J*
602 *Mol Biol* **226**:763–774. doi:10.1016/0022-2836(92)90631-s

603 Sobolevsky AI, Rosconi MP, Gouaux E. 2009. X-ray structure, symmetry and
604 mechanism of an AMPA-subtype glutamate receptor. *Nature* **462**:745–756.
605 doi:10.1038/nature08624

606 Spruston N, Jonas P, Sakmann B. 1995. Dendritic glutamate receptor channels in rat
607 hippocampal CA3 and CA1 pyramidal neurons. *J Physiology* **482**:325–352.
608 doi:10.1113/jphysiol.1995.sp020521

609 Tajima N, Karakas E, Grant T, Simorowski N, Diaz-Avalos R, Grigorieff N, Furukawa
610 H. 2016. Activation of NMDA receptors and the mechanism of inhibition by
611 ifenprodil. *Nature* **534**:63–68. doi:10.1038/nature17679

612 Tang A-H, Chen H, Li TP, Metzbower SR, MacGillavry HD, Blanpied TA. 2016. A
613 trans-synaptic nanocolumn aligns neurotransmitter release to receptors. *Nature*
614 **536**:210–214. doi:10.1038/nature19058

615 Tao C-L, Liu Y-T, Sun R, Zhang B, Qi L, Shivakoti S, Tian C-L, Zhang P, Lau P-M,
616 Zhou ZH, Bi G-Q. 2018. Differentiation and Characterization of Excitatory and
617 Inhibitory Synapses by Cryo-electron Tomography and Correlative Microscopy. *J*
618 *Neurosci* **38**:1493–1510. doi:10.1523/jneurosci.1548-17.2017

619 Tønnesen J, Inavalli VVGK, Nägerl UV. 2018. Super-Resolution Imaging of the
620 Extracellular Space in Living Brain Tissue. *Cell* **172**:1108-1121.e15.
621 doi:10.1016/j.cell.2018.02.007

622 Turk M, Baumeister W. 2020. The promise and the challenges of cryo-electron
623 tomography. *Febs Lett* **594**:3243–3261. doi:10.1002/1873-3468.13948

624 Volgushev M, Vidyasagar TR, Chistiakova M, Eysel UT. 2000. Synaptic transmission in
625 the neocortex during reversible cooling. *Neuroscience* **98**:9–22. doi:10.1016/s0306-
626 4522(00)00109-3

627 Wagner T, Merino F, Stabrin M, Moriya T, Antoni C, Apelbaum A, Hagel P, Sitsel O,
628 Raisch T, Prumbaum D, Quentin D, Roderer D, Tacke S, Siebolds B, Schubert E,
629 Shaikh TR, Lill P, Gatsogiannis C, Raunser S. 2019. SPHIRE-crYOLO is a fast and
630 accurate fully automated particle picker for cryo-EM. *Commun Biol* **2**:218.
631 doi:10.1038/s42003-019-0437-z

632 Wan W, Kolesnikova L, Clarke M, Koehler A, Noda T, Becker S, Briggs JAG. 2017.
633 Structure and assembly of the Ebola virus nucleocapsid. *Nature* **551**:394–397.
634 doi:10.1038/nature24490

635 Watanabe S, Trimbuch T, Camacho-Pérez M, Rost BR, Brokowski B, Söhl-Kielczynski
636 B, Felies A, Davis MW, Rosenmund C, Jorgensen EM. 2014. Clathrin regenerates
637 synaptic vesicles from endosomes. *Nature* **515**:228–233. doi:10.1038/nature13846

638 Whittaker VP. 1959. The isolation and characterization of acetylcholine-containing
639 particles from brain. *Biochem J* **72**:694–706. doi:10.1042/bj0720694

640 Wolf SG, Mutsafi Y, Dadosh T, Ilani T, Lansky Z, Horowitz B, Rubin S, Elbaum M,
641 Fass D. 2017. 3D visualization of mitochondrial solid-phase calcium stores in whole
642 cells. *eLife* **6**:e29929. doi:10.7554/elife.29929

643 Zhu F, Cizeron M, Qiu Z, Benavides-Piccione R, Kopanitsa MV, Skene NG, Koniaris B,
644 DeFelipe J, Fransén E, Komiyama NH, Grant SGN. 2018. Architecture of the Mouse
645 Brain Synaptome. *Neuron* **99**:781-799.e10. doi:10.1016/j.neuron.2018.07.007

646 Zhu S, Gouaux E. 2017. Structure and symmetry inform gating principles of ionotropic
647 glutamate receptors. *Neuropharmacology* **112**:11–15.
648 doi:10.1016/j.neuropharm.2016.08.034

649 Zuber B, Nikonenko I, Klauser P, Muller D, Dubochet J. 2005. The mammalian central
650 nervous synaptic cleft contains a high density of periodically organized complexes.
651 *Proc Natl Acad Sci* **102**:19192–19197. doi:10.1073/pnas.0509527102

652 **Acknowledgements**

653 We would like to thank Christos Savvas, Giuseppe Cannone and Shaoxia Chen for help
654 with maintaining and setting up MRC LMB Titan Krios microscopes. We would like to
655 thank the Astbury Biostructure Laboratory (ABSL), particularly Rebecca Thompson,
656 Emma Hesketh, Dan Maskell, and Helmut Gnaegi for help with setting up and maintaining
657 HPF, cryo-ultramicrotome, cryoFM and Titan Krios microscopes. We are grateful to Jake
658 Grimmett, Toby Darling, Wallace Tudeme, Kerry Kiggins, and Jack Carberry for providing
659 essential computational support. Heather Lloyd, Ilona Rigo, Mel Reay, Danielle Mansfield
660 and Biomedical staff for technical support. Madeleine Gilbert and Eva Martínez Barceló
661 for assistance with annotation of synapse tomograms. Grant funding: An Academy of
662 Medical Sciences Springboard Award (SBF005/1046), UKRI Future Leader Fellowship
663 (MR/V022644/1) and a University of Leeds Academic Fellowship to RAWF. C.L. was

664 funded by a BBSRC White Rose DTP PhD studentship (BB/M011151/1). A Wellcome
665 Trust (Technology Development Grant 202932), the European Research Council (ERC)
666 under the European Union's Horizon 2020 Research and Innovation Programme (695568
667 SYNNOVATE), Simons Foundation for Autism Research Initiative (529085) to SGGN
668 and NHK. Medical Research Council (MC_UP_1201/16) and the European Research
669 Council (ERC) under the European Union's Horizon 2020 research and innovation
670 programme (ERC-CoG-648432 MEMBRANEFUSION), and the Max Planck Society to
671 JAGB. WK was supported by the Medical Research Council (MC_UP_1201/8). ABSL
672 Titan Krios microscopes were funded by the University of Leeds and Wellcome Trust
673 (108466/Z/15/Z). The Leica EM ICE, UC7 ultra/cryo-ultramicrotome and
674 cryoCLEM systems were funded by Wellcome Trust (208395/Z/17/Z).

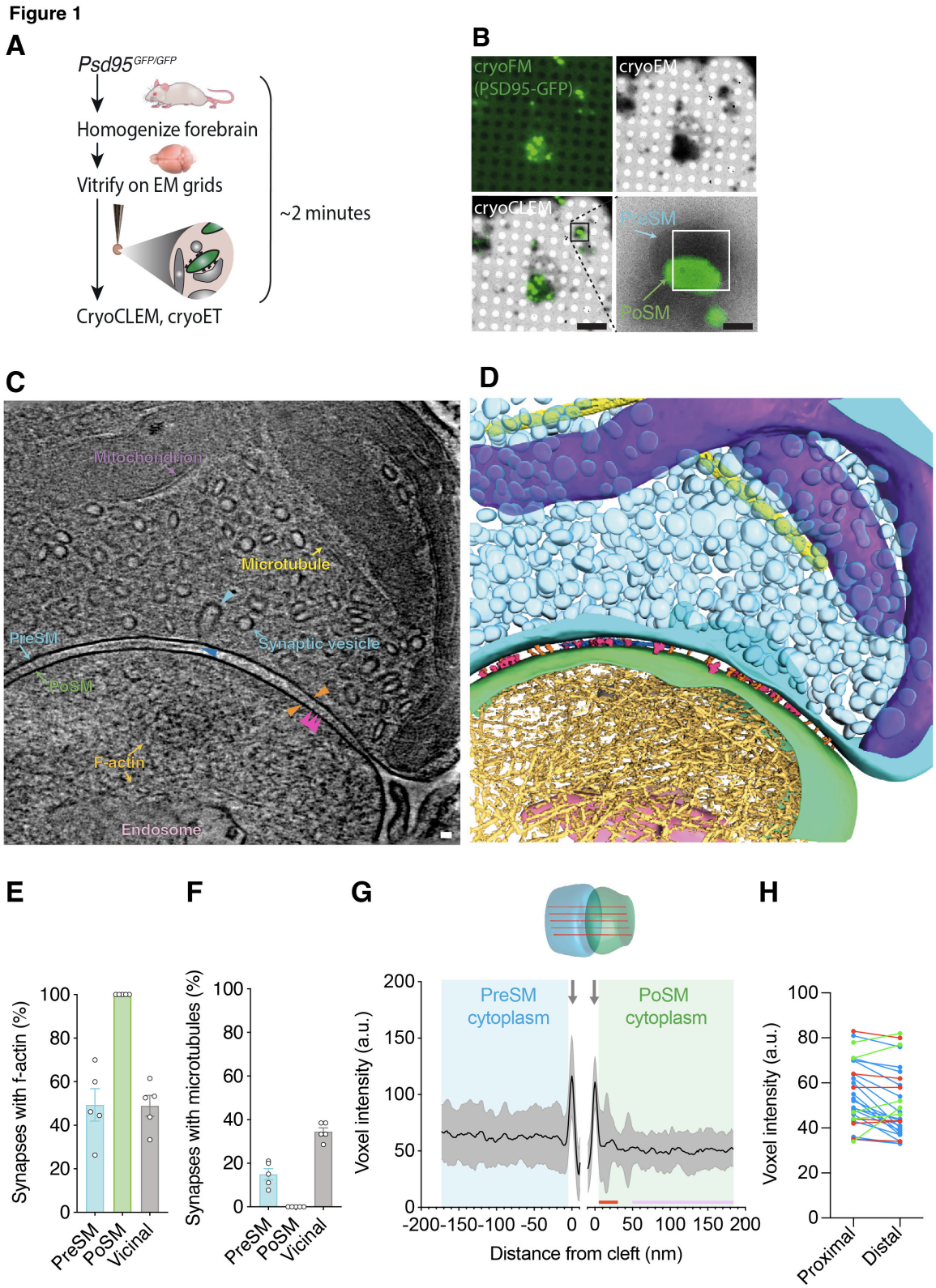

675

676 **Figure 1.** CryoCLEM-targeted cryoET of mouse forebrain synapses.

677 (A) Schematic of the 'ultra-fresh' preparation of synapses for cryoCLEM. *Psd95*$^{GFP/GFP}$
678 knockin mice were culled, forebrain was dissected, homogenized in ice cold artificial
679 cerebrospinal fluid, and plunge-frozen on cryoEM grids. 2 minutes was the time taken to
680 cull, dissect and cryopreserve samples on EM grids.

681 (B) CryoCLEM of cryoEM grid square containing an ultra-fresh synapse preparation. *Top*
682 *left*, cryoFM image of a holey carbon grid square. *Top right*, cryoEM image of the same
683 grid square shown in top left. *Bottom left*, merged image of cryoFM and cryoEM images
684 indicating location of PSD95-GFP puncta. Scale bar, 5 µm. Black box indicates region
685 enlarged in *Bottom right*, showing PSD95-GFP associated with PoSM. White rectangle,
686 indicates region where images for the tomogram shown in C were acquired. Scale bar, 500
687 nm.

688 (C) Tomographic slice of PSD95-containing glutamatergic synapse. The PoSM (green)
689 was identified by PSD-GFP cryoCLEM and the PreSM (cyan) was identified by its
690 tethering to the PoSM and the prevalence of synaptic vesicles. Salient organelle and
691 macromolecular constituents are indicated: Purple arrow, mitochondrion. Yellow arrow,
692 microtubule. Cyan arrow, synaptic vesicle and cyan arrowhead indicating intermediate of
693 vesicle fission/fusion. Gold arrow, F-actin filament. Pink arrow, putative endosomal
694 compartment. Orange arrowheads, transsynaptic macromolecular complex bridging PreSM
695 and PoSM. Magenta arrowheads, postsynaptic membrane proteins with extracellular
696 domains extending 13-14 nm into the synaptic cleft. Blue arrow, lateral matrix of
697 macromolecules in synaptic cleft. Scale bar, 20 nm. The tomographic map shown here is
698 representative of 93 tomograms obtained across 5 mouse forebrain preparations.

699 (D) 3D segmentation of membranes and macromolecules in a representative tomographic
700 volume of a PSD95-containing glutamatergic synapse. Coloured as in C.

701 (E) Prevalence of branched filamentous actin networks in presynaptic membrane
702 compartments (PreSM, cyan), PSD95-containing postsynaptic membrane compartments
703 (PoSM, green), and neighbouring non-synaptic membrane compartments (Vicinal, grey).
704 Data points are per mouse, for 5 adult *Psd95*$^{GFP/GFP}$ mouse forebrain samples. Error bars,

705 SEM.

706 (F) Same as E but for microtubules.

707 (G) Molecular crowding of the PreSM and PoSM cytoplasm in ultra-fresh synapse
708 preparation. *Top*, schematic showing the measurement of molecular density estimated with
709 multiple line profiles plots of voxel intensity within each synapse tomogram. *Bottom*, voxel
710 intensity (a.u., arbitrary units) profile plots of presynaptic (cyan) and postsynaptic (green)
711 cytoplasm. Profiles were aligned to the lipid membrane peak of the PreSM and PoSM (grey
712 arrows). The average intensity profile of 27 synapses from 3 mice is shown in black with
713 1 standard deviation in grey. Red and purple bar, proximal and distal regions of PoSM
714 cytoplasm, respectively, as analysed in H.

715 (H) Comparison of average molecular density profile in regions 5-30 nm (proximal) and
716 50-200 nm (distal) from the PoSM of each synapse. Regions proximal to the PoSM
717 correspond to locations in which a PSD is a conserved feature in conventional EM. Blue,
718 red and green datapoints, synapses with cytoplasm proximal the PoSM that contained
719 significantly higher, lower, and not significantly different density from distal regions,
720 respectively (two-tailed *t* test with Bonferroni correction, $P< 0.05$, n=682 and 5673 voxels).

721 **Figure supplement 1.** CryoFM, docked vesicles and actin in PSD95-GFP-containing synapses.

722 **Figure supplement 2.** Molecular density analysis within synapse tomographic volumes.

723 **Figure supplement 3.** Tomographic slices and molecular density profiles of 27 ultra-fresh PSD95-
724 GFP synapses.

725 **Figure 1–video 1-7.** Reconstructed tomographic volumes of PSD95-GFP-containing ultra-fresh
726 synapses.

727 **Figure 1-table 1.** A spreadsheet detailing the organelle and macromolecular constituents within
728 each tomogram of the ultra-fresh synapse cryoET dataset, including within the PreSM and PoSM
729 of PSD95-GFP containing synapses and additional subcellular compartments in the vicinity.

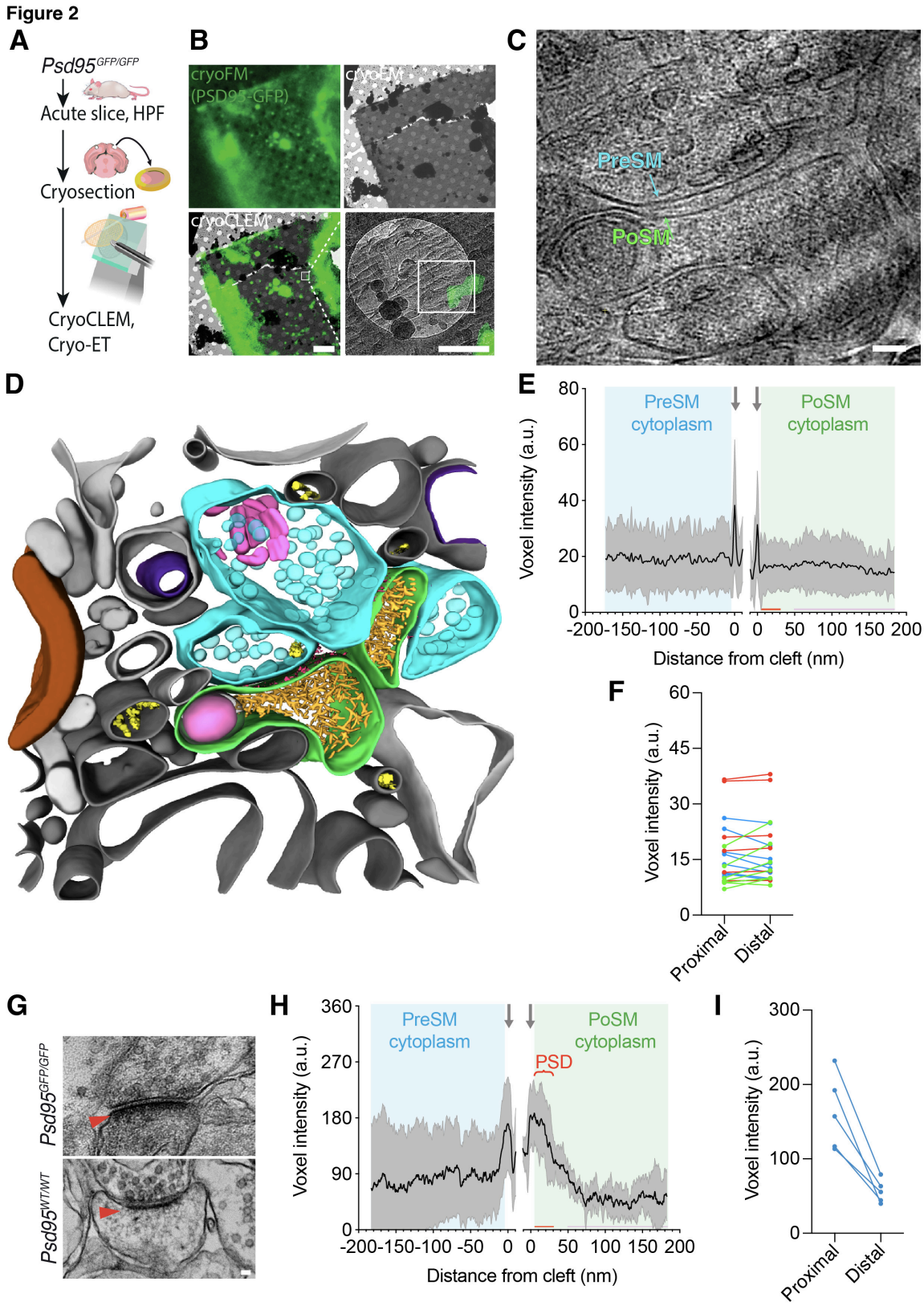

Figure 2. The in-tissue molecular architecture of glutamatergic synapses in the adult

732 mammalian brain.

733 (A) Schematic showing cryoCLEM and cryoET workflow using thin vitreous cryo-sections
734 from forebrains of adult *Psd95*$^{GFP/GFP}$ knockin mice to determine the in-tissue architecture
735 of glutamatergic synapses. Mice were culled and dissected. 100 µm acute slices were
736 collected, from which 2 mm diameter biopsies of cortex were high-pressure frozen. 70-150
737 nm thin vitreous cryo-sections were cut from vitrified tissue and attached to cryoEM grid
738 for cryoCLEM and cryoET.

739 (B) CryoCLEM of cryoEM grid square containing 150 nm thin vitreous cryo-section. *Top*
740 *left*, cryoFM image of a holey carbon grid square. *Top right*, cryoEM image of the same
741 grid square shown in top left. *Bottom left*, merged image of cryoFM and cryoEM images
742 indicating location of PSD95-GFP puncta. Scale bar, 5 µm. Black box indicates region
743 enlarged in *Bottom right*, showing PSD95-GFP associated with PoSM. White box indicates
744 region where images for the tomogram shown in 'c' were acquired. Scale bar, 500 nm.

745 (C) Tomographic slice of PSD95-GFP containing synapse within thin vitreous cryo-section
746 of adult mouse cortex. Cyan, PreSM. Green, PoSM. Scale bar, 50 nm.

747 (D) 3D segmentation of membranes and macromolecules in a representative tomographic
748 volume of a PSD95-containing glutamatergic synapse within thin vitreous cryo-section of
749 adult mouse cortex. The PoSM (green) was identified by PSD-GFP cryoCLEM and the
750 PreSM (cyan) was identified by its tethering to the PoSM and the prevalence of synaptic
751 vesicles. Salient organelle and macromolecular constituents are indicated: Magenta,
752 membrane proteins within synaptic cleft. Purple, mitochondrion. Yellow, microtubule.
753 Pink, putative endosomal compartment. Brown, myelin. Grey, vicinal membrane-bound
754 subcellular compartments.

755 (E) Molecular profiles same as **Figure 1G** but for 21 in-tissue synapses of vitreous cryo-
756 sections from acute brain slices of seven *Psd95*$^{GFP/GFP}$ mice.

757 (F) Comparison of average molecular density profile in regions 5-30 nm (proximal) and
758 50-200 nm (distal) from the PoSM of each synapse. Blue, red and green datapoints,

759 synapses with cytoplasm proximal the PoSM that contained significantly higher, lower,
760 and not significantly different density from distal regions, respectively (two-tailed *t* test
761 with Bonferroni correction, $P < 0.05$, n=682 and 5673 voxels).

762 (G) Conventional EM of synapses in chemically fixed, resin-embedded, heavy metal-
763 stained acute brain slice biopsies from *Psd95*$^{GFP/GFP}$ knockin (left) and wildtype (right),
764 respectively. Red arrowhead, postsynaptic density. Scale bar, 50 nm.

765 (H and I) Same as E and F but for acute brain slice biopsies imaged by conventional EM
766 (chemically fixed, resin imbedded, and heavy metal-stained) from 3 *Psd95*$^{GFP/GFP}$ mice.
767 PSD, postsynaptic density evident in non-native, conventional EM samples.

768 **Figure supplement 1.** Molecular density profiling and tomographic slices of 21 in-tissue vitreous
769 cryo-section tomograms containing PSD95-GFP synapses.

770 **Figure supplement 2.** Conventional EM of adult brain glutamatergic synapses.

771 **Figure 2–video 1-2.** Reconstructed tomographic volumes of in-tissue PSD95-GFP-containing
772 synapses.

773 **Figure 2-table 1.** A spreadsheet detailing the organelle and macromolecular constituents within
774 each tomogram of the in-tissue synapse cryoET dataset, including within the PreSM and PoSM of
775 PSD95-GFP containing synapses and additional subcellular compartments in the vicinity.

Figure 3

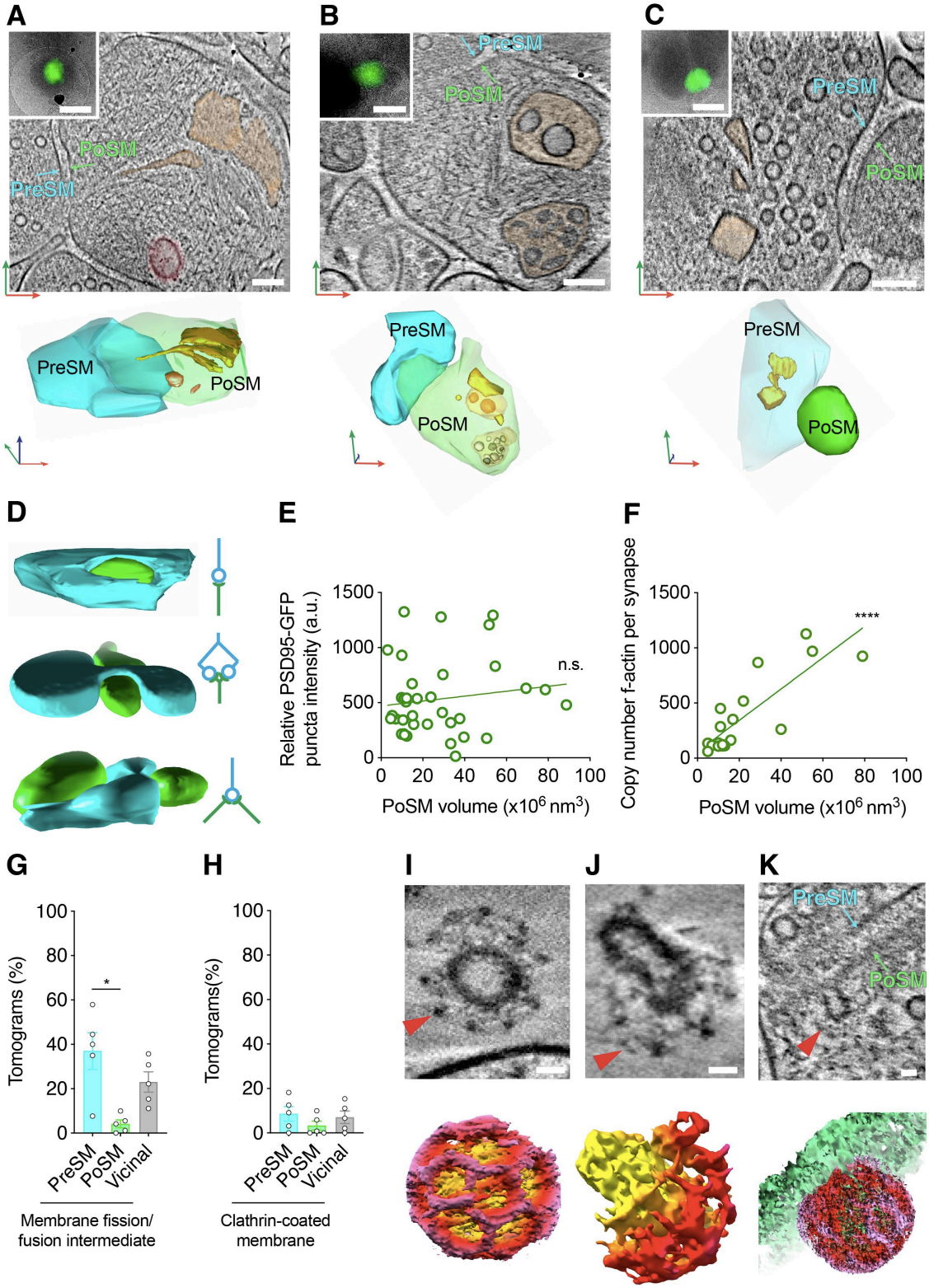

Figure 3. Architecture of lipid membrane bilayers in glutamatergic synapses.

778 (A-C) Organelles in PSD95-containing synapse shown *top*, as a tomographic slice and
779 *bottom*, 3D segmentation. *Top inset,* PSD95-GFP cryoCLEM image of synapse. Scale bar, 500
780 nm. Cyan, PreSM. Green, PoSM. Red, green and blue arrows indicate *x*-, *y*-, and *z*-axis of
781 tomogram, respectively. Scale bar, 100 nm.

782 (A) Flat/tubular membrane compartment and large spheroidal membrane compartment
783 pseudo-coloured orange and red, respectively.

784 (B) Multivesicular bodies pseudo-coloured orange.

785 (C) Polyhedral membrane vesicle pseudo-coloured orange

786 (D) 3D segmentation (*left*) and schematic (*right*) of PSD95-GFP-containing synapses
787 showing various topologies of connectivity. *Top*, unimodal single input and single output.
788 *Middle*, bifurcated synapse with single input and output. *Bottom*, divergent synapse with
789 single input and two outputs. Cyan, PreSM input. Green, PoSM output.

790 (E) Plot of fluorescence intensity (from cryoFM of PSD95-GFP) versus PoSM volume
791 suggesting that there is no correlation between apparent amount of PSD95-GFP and PoSM
792 volume. Linear regression (green line) with Pearson's r=0.14, P=0.41.

793 (F) Plot showing the copy number of F-actin cytoskeletal elements in PoSM compartment
794 versus PoSM volume of each synapse. The copy number of actin filaments was estimated
795 from 3D segmented models of 7 nm filaments within the tomographic map. F-actin
796 branching from another filament were counted as a separate filament. Linear regression
797 (green line) with Pearson's r=0.83, P<0.0001.

798 (G-K) Snapshots and quantification of membrane remodeling within glutamatergic
799 synapses.

800 (G) Prevalence of membrane fission/fusion intermediates within PreSM, PoSM, and non-
801 synaptic membranes (vicinal) from tomograms of 5 adult *Psd95*$^{GFP/GFP}$ mice. Error bars,
802 SEM.*, Paired two-tailed *t* test, P=0.021, n=5 mice)

803 (H) Same as G but for clathrin-coated membrane.

804 (I) *Top*, tomographic slice of a clathrin-coated (red arrowhead) synaptic vesicle and *bottom,*
805 a 3D tomographic density map for the region shown on top. Clathrin cage and membrane
806 is shown with red and yellow voxels respectively. Scale bar, 20 nm.

807 (J) *Top*, tomographic slice of a clathrin-coat (red arrowhead) encapsulating part of an
808 internal membrane within the PreSM compartment of a PSD95-GFP containing synapse
809 and shown *bottom,* a masked 3D tomographic map. Clathrin cage and membrane is shown
810 with red and yellow voxels, respectively. Scale bar, 20 nm.

811 (K) *Top*, tomographic slice, and *bottom*, masked 3D tomographic map showing clathrin-
812 coated endocytic pit (red arrowhead) within the cleft of a PSD95-GFP containing PoSM.
813 Clathrin cage and membrane is shown with red and green voxels, respectively. Scale bar,
814 20 nm.

815 **Figure supplement 1.** Structural categories of membrane-bound organelles in PSD95-containing
816 synapses in the adult brain.

Figure 4

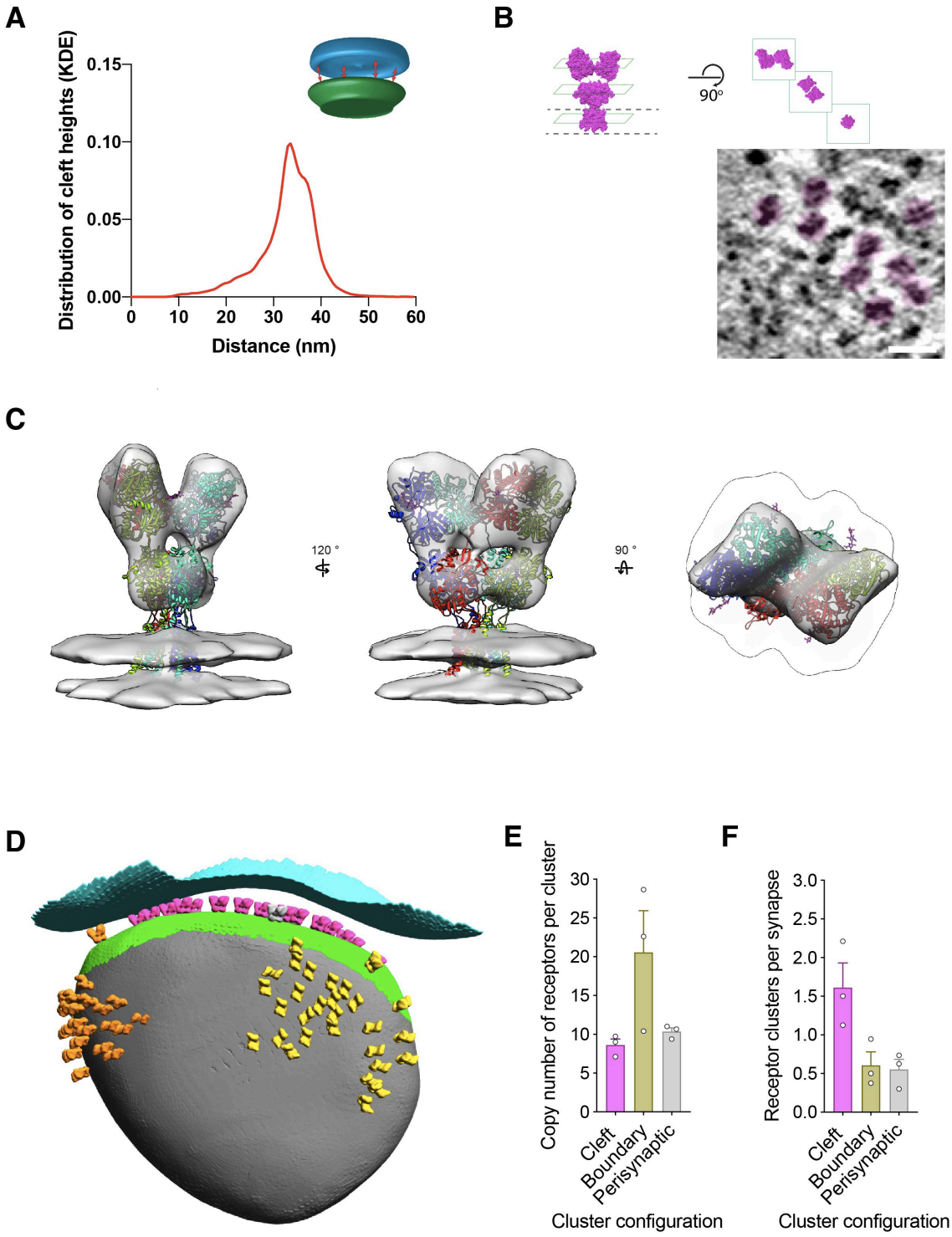

Figure 4. Structural variables of synaptic strength.

819 (A) Distribution of cleft height distances of all synapses is shown as a kernel density
820 estimation (KDE). *Inset*, schematic depicting nearest neighbour method for defining the
821 synaptic cleft between PreSM (cyan) and PoSM (green) compartments.

822 (B) *Top left*, 'side' view of atomic structure of AMPA subtype of ionotropic glutamate
823 receptor (PDB ID: 3kg2). Dashed line, boundary of transmembrane domain. *Top right,*
824 'top' views of distal amino-terminal domain layer, proximal ligand-binding domain layer,
825 and transmembrane domain layer. *Bottom left*, tomographic slice of PSD95-GFP
826 containing membrane oriented approximately parallel to the electron beam. Putative
827 ionotropic glutamate receptor pseudo-coloured in magenta. *Bottom right*, tomographic of
828 PSD95-GFP containing membrane oriented approximately orthogonal to the electron
829 beam. Multiple putative ionotropic glutamate receptor pseudo-coloured in magenta. Scale
830 bar, 20 nm.

831 (C) In situ structure of ionotropic glutamate receptors within PSD95-GFP containing PoSM
832 determined by subtomogram averaging of 2,368 sub-volumes. Atomic model of AMPA
833 receptor (GluA2, PDB: 3kg2) docked in the determined map. Subunits of the model are
834 coloured in red, yellow, cyan and purple.

835 (D) Cluster analysis of identified ionotropic glutamate receptors depicted as a 3D model of
836 the postsynaptic compartment with ionotropic glutamate receptors in the orientation and
837 position determined by sub-tomogram averaging. Each cluster is coloured differently:
838 magenta, orange, and yellow. Presynaptic and postsynaptic cleft membrane are shown in
839 cyan and green, respectively. Postsynaptic membrane outside of the cleft is shown in grey.

840 (E) Receptor number per cluster for three different cluster locations: in the cleft (magenta),
841 partly inside and outside the cleft (boundary, yellow), and completely outside the cleft
842 (perisynaptic, grey) from tomograms of 3 adult *Psd95*$^{GFP/GFP}$ mice.

843 (F) Prevalence of receptor clusters for three different cluster locations: in the cleft
844 (magenta), partly inside and outside the cleft (boundary, yellow), and completely outside
845 the cleft (perisynaptic, grey) from tomograms of 3 adult *Psd95*$^{GFP/GFP}$ mice.

846 **Figure supplement 1.** Quantification and variability of cleft height in glutamatergic synapses.

847 **Figure supplement 2.** Subtomogram averaging and anchoring of ionotropic glutamate receptors.

848 **Methods**

849 **Mouse genetics and breeding**

850 Animals were treated in accordance with UK Animal Scientific Procedures Act (1986) and
851 NIH guidelines. The generation and characterization of the PSD95-GFP knockin mouse
852 (*Psd95*^{GFP}) was described (Broadhead et al., 2016; Zhu et al., 2018). The endogenous
853 PSD95 protein levels, assembly into supercomplexes, anatomical localization,
854 developmental timing of expression and electrophysiological function in the hippocampus
855 CA1-CA3 synapses in *Psd95*^{GFP} mice are indistinguishable from WT mice (Broadhead et
856 al., 2016; Frank et al., 2016; Zhu et al., 2018).

857 **Ultra-fresh synapse preparation**

858 Samples were prepared from 5 adult (P65-P100) male *Psd95*$^{GFP/GFP}$ knockin mice. Sample
859 preparation from culling to cryopreservation of each mouse was less than 2 minutes. Mice
860 were culled by cervical dislocation. Forebrain, including cortex and hippocampus, that
861 encompass the known diversity glutamatergic synapses (Zhu et al., 2018) were removed
862 (in <40 s) and were homogenized (<20 s) by applying 12 strokes of a Teflon-glass pestle
863 and mortar containing 5 ml ice-cold (~1 °C) carbogenated (5% CO_2, 95% O_2) artificial
864 cerebrospinal fluid (ACSF; 125 mM NaCl, 25 mM KCl, 25 mM $NHCO_3$, 25 mM glucose,
865 2.5 mM KCl, 2 mM $CaCl_2$, 1.25 mM NaH_2PO_4, 1 mM $MgCl_2$; Osmolality: 310 mOsM/L).
866 Ice-cold ACSF was used to limit mechanical stimulation since synaptic transmission and
867 other enzyme-catalyzed processes (e.g. endocytosis) are negligible at this temperature
868 (Volgushev et al., 2000). 1 µl homogenate was diluted into 100 µl ice-cold ACSF
869 containing 1:6 BSA-coated 10 nm colloidal gold (BBA; used as a fiducial maker) (<10 s).
870 3 µl sample was applied onto glow-discharged 1.2/1.3 carbon foil supported by 300-mesh
871 Au or Cu grids (Quantifoil) held at 4°C, 100% humidity in Vitrobots (Mark IV, Thermo
872 Fisher). Excess sample was manually blotted from the non-foil side of the grid for ~4s with
873 Whatman paper (No. 1; manipulated within the Vitrobot with tweezers) before
874 cryopreserving by plunge freezing in liquid ethane held at -180ºC (*57*). 1-2 grids were
875 prepared from each mouse on 1-2 Vitrobots.

876

877 **In-tissue acute slice synapse preparation**

878 Samples were prepared from 6 adult (P65-P100) male *Psd95*$^{EGFP/EGFP}$ knockin mice. Mice
879 were culled by cervical dislocation. Forebrain, including cortex and hippocampus, were
880 removed and 100 µm coronal acute slices were prepared in cutting buffer (93 mM N-
881 methyl-D-glucamine, 2.5 mM KCl, 1.2 mM NaH2PO4, 30 mM NaHCO3, 20 mM HEPES,
882 5 mM Sodium ascorbate, 2 mM Thiourea, 3 mM Sodium Pyruvate, 10 mM MgSO4, 0.5
883 mM CaCl2, pH 7.39-7.40, osmolarity 305-315 mOsm/L) using a Leica VT1200S
884 vibratome at 0.5-2°C. Tissue biopsies of acute slices were collected following the method
885 established by Zuber and co-workers in which samples remain viable (Zuber et al., 2005).
886 Briefly, slices were recovered in ACSF perfused with carbogen at room temperature for 45
887 minutes. Next, biopsies were collected with a 2 mm biopsy punch and were transferred to
888 carbogenated NMDG cutting buffer supplemented with 20% dextran 40,000. Biopsies
889 were high-pressure frozen within cryoprotectant into 3 mm carriers using a Leica EM ICE.
890 Tissue was cut into 70-150 nm thick vitreous cryo-sections using a Leica FC7 cryo-
891 ultramicrotome with a CEMOVIS diamond knife (Diatome) from regions of the tissue that
892 were ~25 µm from the vibratome cutting edge. Vitreous cryo-sections were attached to
893 cryoEM grids at -150ºC.

894

895 **Cryogenic correlated light and electron microscopy**

896 Cryogenic fluorescence microscopy (cryoFM) was performed on the Leica EM cryoCLEM
897 system with a HCX PL APO 50x cryo-objective with NA = 0.9 (Leica Microsystems), an
898 Orca Flash 4.0 V2 sCMOS camera (Hamamatsu Photonics), a Sola Light Engine
899 (Lumencor) and the following filters (Leica Microsystems): green (L5; excitation 480/40,
900 dichroic 505, emission 527/30), red (N21; excitation 515-560, dichroic 580, emission LP
901 590), and far-red (Y5; excitation 620/60, dichroic 660, emission 700/75). During imaging,
902 the humidity of the room was controlled to 20-25% and the microscope stage was cooled
903 to -195°C. Ice thickness was assessed with a brightfield image and L5 filter. Regions of the

904 grid with thin ice (~50%) were imaged sequentially with the following channel settings:
905 0.4 s exposure, 30% intensity in green channel; 40 ms exposure, intensity 11% in BF
906 channel; 0.4 s exposure, 30% intensity in red channel, 0.4 s exposure, 30% intensity in far-
907 red channel. 0.3 µm separated z-stack of images was collected for each channel over a 5-
908 20 µm focal range. Images were processed in Fiji. The location of PSD95-GFP was evident
909 as puncta of varying brightness that were exclusively in the green channel. The occasional
910 autofluorescent spot was identifiable by fluorescence across multiple channels, including
911 green and red channels. Grid squares were selected for cryoCLEM that contained PSD95-
912 GFP puncta within the holes of the holey carbon grid.

913 **Cryogenic electron microscopy and tomography**

914 CryoEM and CryoET data collection was performed on a Titan Krios microscope (FEI)
915 fitted with a Quantum energy filter (slit width 20 eV) and a K2 direct electron detector
916 (Gatan) running in counting mode with a dose rate of ~4 e^-/pixel/second at the detector
917 level during tilt series acquisition. Intermediate magnification EM maps of the selected grid
918 squares were acquired at a pixel size of 5.1 nm. Using these intermediate magnification
919 maps of each grid square and the corresponding cryoFM image, the location of PSD95-
920 GFP puncta was manually estimated; performing computational alignment of cryoFM and
921 cryoEM images before tomogram acquisition was not necessary.

922 An unbiased tomographic data collection strategy was followed guided by the location
923 PSD95-GFP cryoCLEM data. 93 ultra-fresh and 50 acute slice/in-tissue (vitreous cryo-
924 section) PSD95-GFP synapse tomograms were collected from 5 and 6 mice respectively.
925 No PSD95-GFP tomograms were excluded from the dataset (**Figure 1–table 1** and **Figure**
926 **2–table 1**). Tomographic tilt series of the cryoFM-correlated PSD95-GFP locations were
927 collected between ±60° using a grouped dose-symmetric tilt scheme (Hagen et al., 2017)
928 in serialEM (Mastronarde, 2005) and a phase plate (Fukuda et al., 2015) pre-conditioned
929 for each tomogram. Groups of 3 images with 2° increments were collected. Images with a
930 2 s exposure with 0.8-1.25 µm nominal defocus at a dose rate of ~0.5 e^-/Å/s were collected
931 as 8x 0.25 s fractions, giving a total dose of ~60 e^-/Å over the entire tilt series at a calibrated
932 pixel size of 2.89 Å. This pixel size corresponds to a field of view of 1.3 μm^2. Consequently,

933 the centres of all synapses were captured in the tomographic dataset and synapses with a
934 maximum dimension under 1.3 µm were contained entirely within the tomogram.
935 Tomograms of thin vitreous cryo-sections were collected with the same protocol, but
936 replacing the phase plate with 100 µm objective aperture and acquiring tilt series images at
937 5-6 µm nominal defocus with a nominal pixel size of 3.42 Å.

938 **Conventional EM**

939 Samples were prepared from adult (P65-P100) male *Psd95*$^{EGFP/EGFP}$ knockin and wildtype
940 mice from three sources: i) Fresh 2 mm diameter biopsy samples of the primary or
941 secondary somatosensory cortex were collected from acute brain slices (as described
942 above) and were fixed with chemi-fix buffer composed of 4% paraformaldehyde 2%
943 glutaraldehyde in 50 mM phosphate (PB) pH7.4 for 1 hour. ii) Ultra-fresh synapses were
944 prepared (as described above) and incubated in chemi-fix buffer for 40 min at room
945 temperature. iii) Anesthetized mice were cardiac perfused with 20 ml PB, followed by 40
946 ml chemi-fix buffer. 100 µm coronal sections were collected from the whole brain with a
947 vibratome, from which 2 mm biopsy samples of the cortex were collected and incubated in
948 chemi-fix buffer at 4°C overnight.

949 All samples were next washed three times in PB for 1 minute before post-fixation in 2%
950 osmium tetroxide for 1 hour at room temperature. Next, samples were washed three times
951 in PB for 1 minute each and once in 50% ethanol for 1 minute. Samples were next stained
952 with 4% w/v uranyl acetate in 70% for 1 hour at room temperature before dehydration with
953 sequential washes in 70% ethanol, 90% ethanol, 100% ethanol, 100% acetone for 5 minutes
954 each. Samples were resin embedded by washing twice with propylene oxide for 20 minutes
955 before incubation in 50% araldite epoxy resin in propylene oxide at room temperature
956 overnight. Finally, samples were incubated twice in epoxy resin for 10-16 hours before the
957 resin was polymerized in a mold at 60 °C for 3 days. Ultrathin (80-100 nm) sections
958 collected from with an ultramicrotome were placed on 3.05-mm copper grids, stained with
959 saturated uranyl acetate for 30 minutes, and Reynold's lead citrate for 5 minutes and
960 imaged on a Tecnai F20 TEM at 5,000x and 29,000x magnification.

961 **CryoCLEM image processing**

962 Computational correlation between the cryoFM and cryoEM images was conducted using
963 custom Matlab (Mathworks) scripts as described previously (Kukulski et al., 2011; Schorb
964 and Briggs, 2014). The centre points of at least 10 holes in the holey-carbon foil around
965 each PSD95 position were used as fiducial markers to align the green channel cryoFM
966 image to a montaged intermediate magnification EM image covering the whole grid square.
967 All GFP puncta correlated within membrane-bound compartments with an apparent
968 presynaptic membrane attached to the postsynaptic membrane. The identity of presynaptic
969 membranes was confirmed by the presence of numerous synaptic vesicles.

970 To quantify relative amount of PSD95 in each synapse, PSD95-EGFP puncta in cryoFM
971 images were segmented using the watershed algorithm in ImageJ, from which the pixel
972 intensities of each puncta were integrated.

973 **Tomogram reconstruction**

974 Frames were aligned and ultra-fresh synapse tomograms were reconstructed using 10-20
975 tracked 10 nm fiducial gold markers in IMOD (Kremer et al., 1996). Tomograms of
976 synapses in thin vitreous cryo-sections were aligned by patch tracking and denoised using
977 SPIRE-crYOLO (Wagner et al., 2019). Tomograms used for figures, particle picking,
978 annotation of macromolecular constituents and molecular density analysis were generated
979 with 5 iterations of SIRT and binned to a 11.94 Å (binned 4x). Weighted back-projection
980 tomograms (binned 4x and 2x) were used for subtomogram averaging (see below).

981 **Annotation and analysis of macromolecular constituents in tomograms**

982 Annotation described in **Figure 1–table 1** was performed blind by two curators to assess
983 ultra-fresh synapse structures in IMOD. First, each curator annotated all SIRT
984 reconstructed tomograms independently. Next, a third curator inspected and certified each
985 annotation. The PoSM was identified using PSD95-GFP cryoCLEM (see above). The
986 PreSM was identified as the membrane compartment attached to the PoSM via
987 transsynaptic adhesion proteins and containing numerous synaptic vesicles. Docked

988 synaptic vesicles were defined as vesicles connected 2-8 nm from the PreSM via
989 macromolecular tethers. The average diameter of synaptic vesicles was 40.2 nm and the
990 minimum and maximum dimensions ranged from 20 to 57.8 nm, measured from the outside
991 of the vesicle that included ellipsoidal synaptic vesicles similar to those previously reported
992 (Tao et al., 2018). To assess potential mechanical damage to the native architecture of ultra-
993 fresh synapses, the PoSM or PreSM compartment categorized as either open or closed. An
994 open PreSM or PoSM compartment indicated that the plasma membrane was ruptured,
995 whereas closed PreSM and PoSM compartments were similar to structures obtained from
996 vitreous cryo-sections, indicating the native architecture was retained. Only synapses
997 tomograms with closed PreSM or PoSM were used for further analysis of the molecular
998 architecture and constituents of synapses.

999 Organelles, intermediates of membrane fission or fusion, and identifiable macromolecules
1000 were annotated within the presynaptic, postsynaptic and non-synaptic (vicinal)
1001 compartments within the tomogram dataset (**Figure 1–table 1**), which were classified as
1002 follows: 1) Flat/tubular membrane compartments: Flat membrane tubules 12-20 nm wide
1003 with ≥180° twist along the tubule axis. 2) Large spheroidal membrane compartments:
1004 Vesicles with a diameter greater than 60 nm. 3) Multivesicular bodies: Membranous
1005 compartments containing at least one internal vesicle. 4) Polyhedral vesicles: Membranous
1006 compartment composed of flat surfaces related by ≤90° angle. 6) Dense-cored vesicles. 7)
1007 Fission/fusion intermediates: hemifusion intermediates, protein-coated invaginations of
1008 membrane. 8) Clathrin-coated intermediates: invaginations with a protein coat containing
1009 pentagonal or hexagonal openings. 9) Mitochondria: double membrane with cristae and
1010 electron-dense matrix. 10) Mitochondrial intermediates: mitochondria with budding outer
1011 membrane or putative mitochondrial fragments wrapped by two membrane bilayers. 11)
1012 Ribosomes: 25-35 nm electron dense particles composed of small and large subunits. 12)
1013 F-actin: ~7 nm diameter helical filaments. In the PoSM, F-actin formed a network with
1014 ~70° branch points (**Figure 1–figure supplement 1C)** likely formed by Arp2/3, as
1015 expected(Fäßler et al., 2020; Pizarro-Cerdá et al., 2017). Putative filament copy number in
1016 the PoSM was estimated by manual segmentation in IMOD. 13) Microtubules: ~25 nm
1017 diameter filaments. 14) Cargo-loaded microtubules: vesicles attached to microtubules via

1018 25-30 nm protein tethers.

1019 **Molecular density profile analysis**

1020 Molecular density analysis (Smith and Langmore, 1992) of the PreSM and PoSM
1021 compartments from ultra-fresh synapse and in-tissue vitreous cryo-section tomograms was
1022 carried out using voxel intensity line profiles of the presynaptic and postsynaptic membrane
1023 measured using IMOD, Fiji, and custom scripts. Only PSD95-GFP-labelled synapse
1024 tomograms were analysed and tomograms were only excluded from analysis if they were
1025 oriented on the missing wedge, or if ice contamination, EM grid carbon or cutting damage
1026 obscured the PoSM cytoplasm (see **Figure 1–figure supplement 3** and **Figure 2–figure**
1027 **supplement 1B** showing tomographic slices of each ultra-fresh and in-tissue synapse
1028 tomogram, respectively). All profiles were made at central regions of each synapse,
1029 containing docked presynaptic vesicles and clusters of ionotropic glutamate receptors
1030 (**Figure 1–figure supplement 3**), because this is where the PSD is consistently located in
1031 synapses imaged by conventional EM. Line profiles (36 nm wide and 450 nm long) from
1032 31 single tomographic slices from synapses with PoSM and PreSM oriented on the *z*-axis
1033 of the tomographic volume were measured. Note, projecting multiple tomographic slices,
1034 often used to analyse molecular density of the synapse, will only provide accurate profiles
1035 of the cytoplasm if the PoSM is perfectly oriented in the *z*-direction of the tomographic
1036 volume. Inspecting the line profiles of each tomographic slice showed that the majority
1037 tomograms contained synapses that were slightly tilted with respect to the *z*-axis (**Figure**
1038 **1–figure supplement 2A-B**). We observed that projections of these synapses caused the
1039 PoSM membrane to smear resulting in erroneous cytoplasmic profiles that contained
1040 molecular density from the membrane itself (**Figure 1–figure supplement 2C**). This
1041 highlighted a risk of projecting multiple tomographic slices to measure molecular density
1042 within a specific compartment. We therefore avoided directly generating a 2D projection
1043 of multiple tomographic slices of each tomographic volume. Instead, to avoid this error,
1044 individual profiles of each tomographic slice were aligned to the plasma membrane peak
1045 before profiles were averaged to estimate the relative density of molecular crowding within
1046 sub-volumes of the PreSM and PoSM compartments of each synapse (**Figure 1–figure**
1047 **supplement 2D**). Tomographic slices in which the PoSM was tilted in the *x*-*y* plane relative to

1048 the majority of slices were also excluded from the profile (**Figure 1–figure supplement 2B,**
1049 **top panel)**.To ensure molecular density analysis was capable of detecting a PSD, similar
1050 line profiles were taken from samples prepared for conventional EM (see sample
1051 preparation details below, **Figure 2H** and **Figure 2–figure supplement 2**) as a positive
1052 control.

1053 **Quantitative analysis of the PreSM, PoSM, and synaptic cleft**

1054 Each membrane was segmented in Dynamo (Castaño-Díez et al., 2017), generating 4,000-
1055 20,000 coordinates for each membrane. To refine the contouring of the membrane,
1056 subtomograms of the membrane were refined against an average. The synaptic cleft was
1057 defined computationally using custom Matlab-based script that identifies the nearest
1058 neighbour coordinates between PreSM and PoSM, and vice versa. This gave a dataset of
1059 cleft height distances for each synapse, in which more than 99% of measurements were
1060 distributed within a range of 10-45 nm and none were greater than 60 nm. The distribution
1061 of cleft height distances was plotted using Kernal Density Estimation in Matlab.

1062 **Subtomogram averaging**

1063 Subtomogram alignment and averaging was performed using Matlab-based scripts derived
1064 from the TOM (Nickell et al., 2005) and Av3 (Förster et al., 2005) toolboxes, essentially
1065 as previously described (Wan et al., 2017) using initial datasets from only the first 3 mice.

1066 Coordinates of putative ionotropic glutamate receptors were manually picked in UCSF
1067 Chimera (Pettersen et al., 2004) using two times binned tomograms with an effective voxel
1068 size of 11.94 Å. All membrane proteins with a long-axis extending ~14 nm out of the
1069 membrane and an apparent two-fold symmetry axis were picked. The orientation of the
1070 normal vector to the membrane surface was determined to define the initial orientation of
1071 each subtomogram. The Euler angle defining the final in-plane rotation angle (phi in the
1072 av3 annotation) was randomized. The full set of subtomogram positions was split into two
1073 independent half sets one for all odd and one for all even subtomogram numbers. The two
1074 half sets were processed independently. For initial alignment and averaging, subtomograms
1075 with a box size of 64x64x64 voxels (~76.4x76.4x76.4 nm^3) were extracted from the

1076 respective tomograms and averaged. The initial average shows a long, thin stalk. After one
1077 iteration of alignment using a low pass filter of 30 Å and a complete in-plane angular
1078 search, two-fold symmetry was applied for further iterations. During all steps of alignment
1079 and averaging, the missing wedge was modelled as the sum of the amplitude spectra
1080 determined from 100 randomly seeded noise positions for each tomogram. After 6
1081 iterations subtomograms with a box size of 96x96x96 voxels (~53.7x53.7x53.7 nm^3) were
1082 re-extracted from tomograms with a voxel size of 5.97 Å. Subtomogram positions were
1083 reprojected onto the respective tomogram for visual inspection, and mis-aligned
1084 subtomogram positions as well as subtomograms that had converged to the same position
1085 were removed, reducing the final number of subtomograms to 2368 subtomograms
1086 (odd=1182 and even=1186). The two averages were then further refined for 4 iterations
1087 using a cylindrical mask tightly fit around the obtained structure and including the
1088 membrane and subsequently for 6 more iterations using a cylindrical mask excluding the
1089 membrane. To evaluate the final average and assess the resolution obtained, the averages
1090 from the two half sets were aligned to each other and the FSC was calculated as described
1091 in (Chen et al., 2013) indicating a final resolution of 25 Å (**Figure 4–figure supplement**
1092 **2A**). To test if CTF correction of the data would improve the reconstruction obtained from
1093 subtomogram averaging, the defocus for each tilt image was determined using CTFFIND4
1094 including phase shifts and the defocus estimate was visually checked against the power spectrum
1095 of the tilts. Using the determined defocused values CTF-corrected tomograms were generated in
1096 NovaCTF. Subtomograms were then reextracted from bin2 CTF-corrected tomograms, averaged
1097 and aligned. Neither resolution nor map quality improved over the non CTF corrected data and
1098 therefore ultimately the map from the non-CTF corrected data was used as the final map.

1099 The previously reported atomic coordinates of an AMPA subtype ionotropic glutamate
1100 receptor (Sobolevsky et al., 2009) (PDB: 3KG2) and NMDA receptor (PDB:5fxh)(Tajima
1101 et al., 2016) were fitted as a rigid body into the final subtomogram averaging map using
1102 the fit in map tool in UCSF Chimera. The former was a better fit in keeping with the
1103 expected higher abundance of AMPA receptors at the synapse (Lowenthal et al., 2015;
1104 Spruston et al., 1995).

1105

1106 **Cluster analysis**

1107 Clustering analysis of glutamate receptors was performed using the DBSCAN algorithm
1108 (minimal cluster size 4 and maximal distance between receptors of 70 nm) where the
1109 distances between pairs of receptors were defined as the shortest distance between their
1110 projections on the surface of the membrane. The mesh associated to the surface was
1111 estimated using the "MyOpenCrust" implementation of the crust meshing method and
1112 simplified using the reducepatch from Matlab. The distances between the projected
1113 coordinates were computed using the Dijkstra algorithm on the graph associated to the
1114 mesh.

1115 We computationally categorised receptor clusters that were situated inside the cleft, in
1116 perisynaptic locations outside the cleft, or spanning the boundary of the synaptic cleft. If
1117 perisynaptic clusters arose because of detachment of the PoSM and PreSM during sample
1118 preparation, we would expect to find at least a small population of PSD95-GFP containing
1119 postsynaptic compartments that were not adhered to a pre-synaptic membrane. Examining
1120 every single PSD95-GFP puncta in our cryoCLEM dataset of 93 synapses marked a
1121 postsynaptic membrane that was also attached to a presynaptic membrane, suggesting
1122 synaptic contacts are established in the brain with a high avidity that is not affected by
1123 sample preparation.

1124 **Data availability**

1125 Subtomogram average maps have been deposited in the Electron Microscopy Data Bank
1126 (EMDB) under accession code EMD-53528. Tilt series and 4x binned tomographic
1127 volumes of 'ultra-fresh' and in-tissue synapses (**Figure 1–table 1** and **Figure 2–table 1**)
1128 and segmentation coordinates have been deposited in the Electron Microscopy Public
1129 Image Archive (EMPIAR) with the accession code EMPIAR-12795.

1130

Figure 1-figure supplement 1

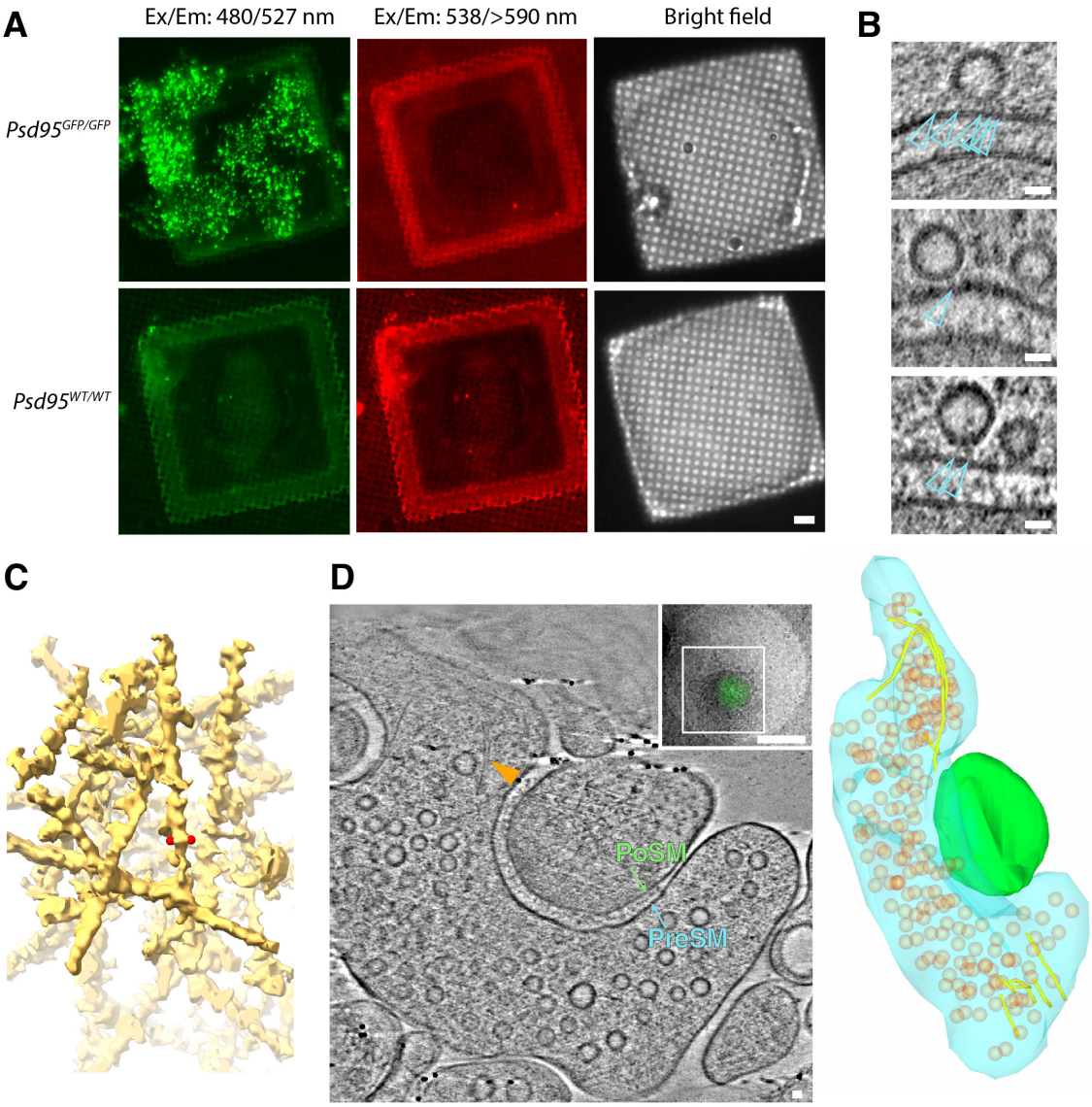

1131

1132 **Figure 1–figure supplement 1.** CryoFM, docked vesicles and actin in PSD95-GFP-containing
1133 synapses.

1134 (A) Cryogenic fluorescence microscopy of forebrain (cortex and hippocampus) ultra-fresh synapse
1135 preparation from *Psd95*$^{GFP/GFP}$ (*top panels*) and WT (*bottom panels*). *Left*, detection of GFP with
1136 excitation and emission filters of 480 nm and 527 nm, respectively. *Middle*, detection of red
1137 fluorescence with excitation and emission filters of 538 nm and >590 nm, respectively. *Right*, bright
1138 field image. Submicron-sized puncta in the GFP channel only detected exclusively in *Psd95*$^{GFP/GFP}$
1139 samples.

1140 (B) Tomographic slice showing representative docked synaptic vesicles. Docked synaptic vesicles
1141 were identified by the macromolecular complexes (open cyan arrow heads) that tethered synaptic
1142 vesicles 2-8 nm from the presynaptic membrane. 96% PreSM compartments contained docked
1143 synaptic vesicles (see **Figure 1–table 1**). Scale bars, 20 nm.

1144 (C) Masked tomographic map of a branched filamentous actin (F-actin) network in PSD95-
1145 containing PoSM compartment. Red spherical markers, spaced 7.1 nm apart on the outside edges
1146 of a filament.

1147 (D) Molecular architecture of F-actin in the presynaptic compartment.

1148 *Left*, tomographic slice through tomogram of synapse located by PSD95-GFP cryoCLEM. F-actin
1149 parallel bundle indicated by yellow arrowhead within PreSM (cyan) compartment that was adhered
1150 to PoSM (green). See also **Figure 1–video 2**. *Top inset*, PSD95-GFP cryoCLEM image of synapse.
1151 White box, indicates White box, indicates region where images for the tomogram were collected.
1152 Scale bar, 500 nm.

1153 *Right*, 3D segmented model of F-actin (yellow tubes) in PreSM (cyan) opposing PoSM (green).
1154 Synaptic vesicles (orange). Short F-actin filaments connect a fraction of synaptic vesicles to the
1155 plasma membrane. Scale bar, 20 nm.

Figure 1-figure supplement 2

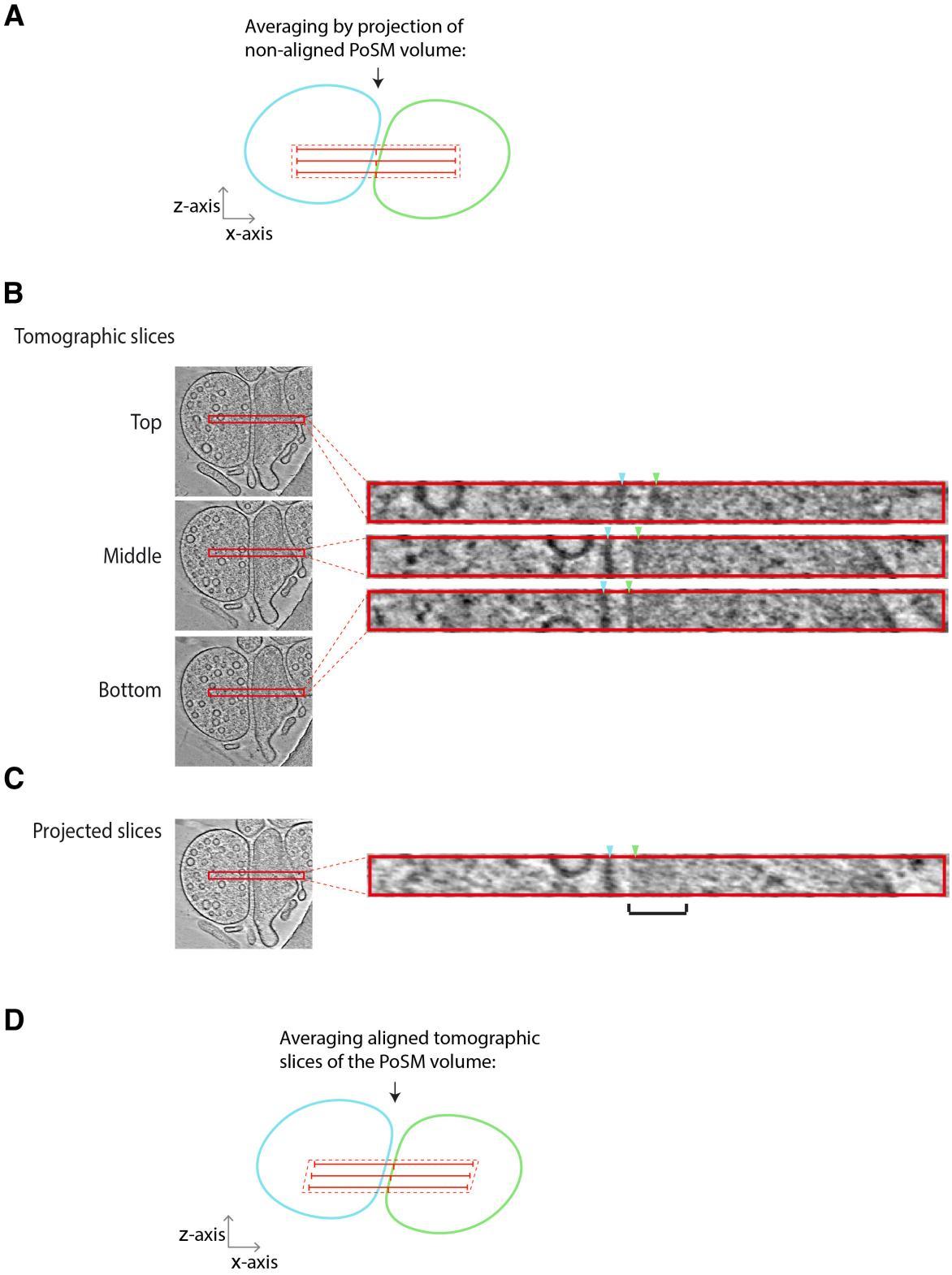

1156

1157 **Figure 1–figure supplement 2.** Molecular density analysis within synapse tomographic volumes.

1158 (A) Schematic showing an error that arises when projecting a tomographic volume of synapse with
1159 a pre- (blue) and post-synaptic (green) compartments that are not perfectly aligned with the *z*-axis
1160 of the tomogram. Molecular crowding has been previously analysed using a projection (hatched
1161 red rectangle) of multiple tomographic slices (red lines). Projection of such an unaligned volume
1162 generates an erroneous molecular density profile in which the plasma membrane and extracellular
1163 proteins contribute to measurements of the postsynaptic cytoplasm. Black arrow, direction of the
1164 missing wedge.

1165 (B) Example of synapse tomographic volume with postsynaptic membrane not perfectly oriented
1166 with z-axis. *Left* and *right*, tomographic slices sub-volume (red rectangle) of top, middle and bottom
1167 of tomographic sub-volume, respectively. Blue and green arrowheads, position of PoSM and
1168 PreSM in each tomographic slice of the sub-volume, respectively. Note, the position of the PoSM
1169 changes in different slices of the sub-volume.

1170 (C) Projection of unaligned tomographic slices with black bracket showing error caused by regions
1171 of molecular density from the membrane and synaptic cleft smeared into the postsynaptic
1172 cytoplasm

1173 (D) Schematic showing how accurate measurements of molecular density of the postsynaptic
1174 cytoplasm within a tomographic sub-volume were obtained (**Figure 1G-H** and **2E-F**). See also
1175 detailed description in methods section 'molecular density profile analysis'. To measure molecular
1176 density profiles of each tomographic slice were aligned to the PoSM before averaging.
1177 Tomographic slices in which the PoSM was tilted in the *x-y* plane (see top tomographic slice in
1178 panel B) were also excluded from the profile.

Figure 1-figure supplement 3

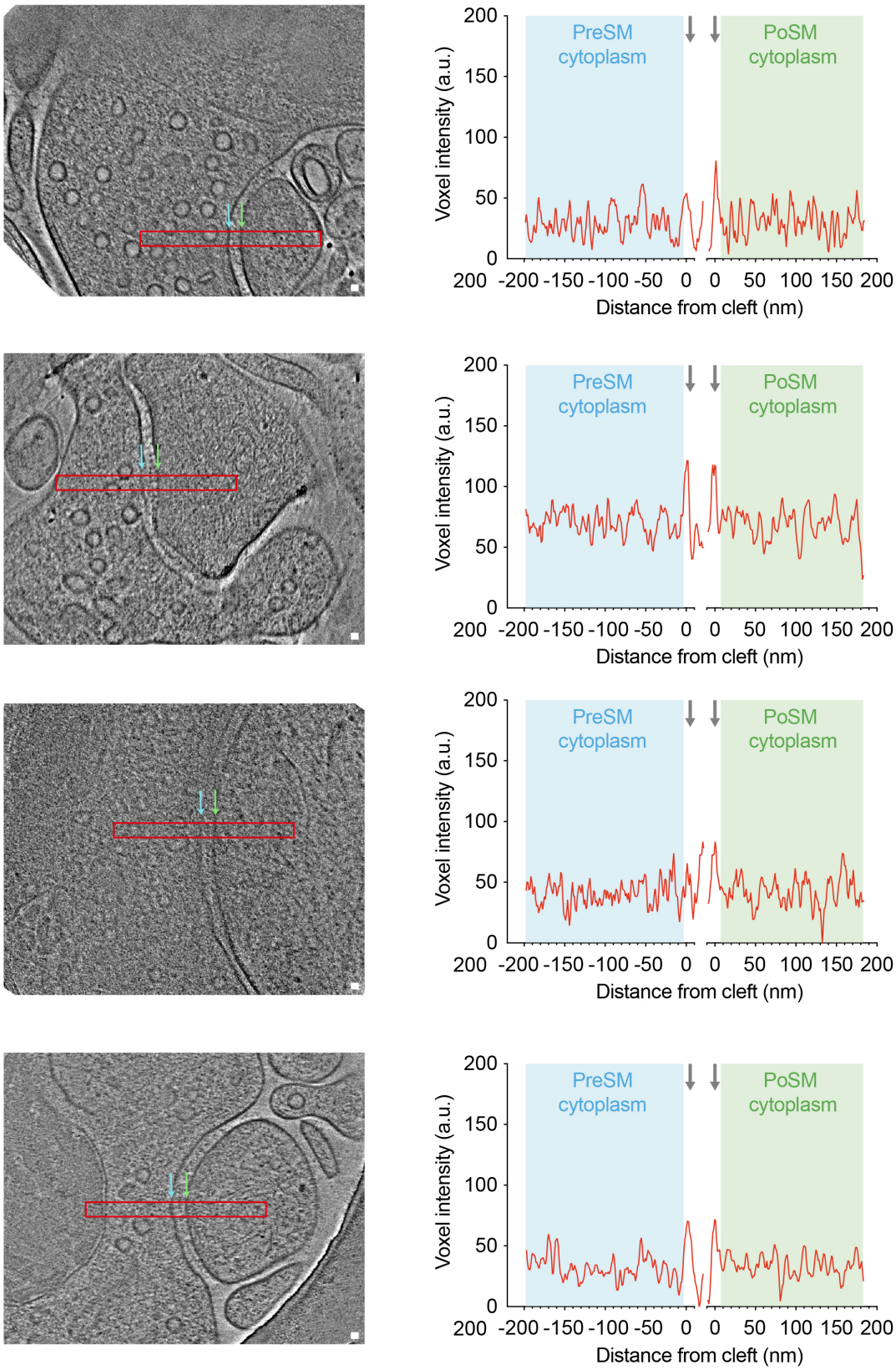

1179

Figure 1-figure supplement 3 cont.

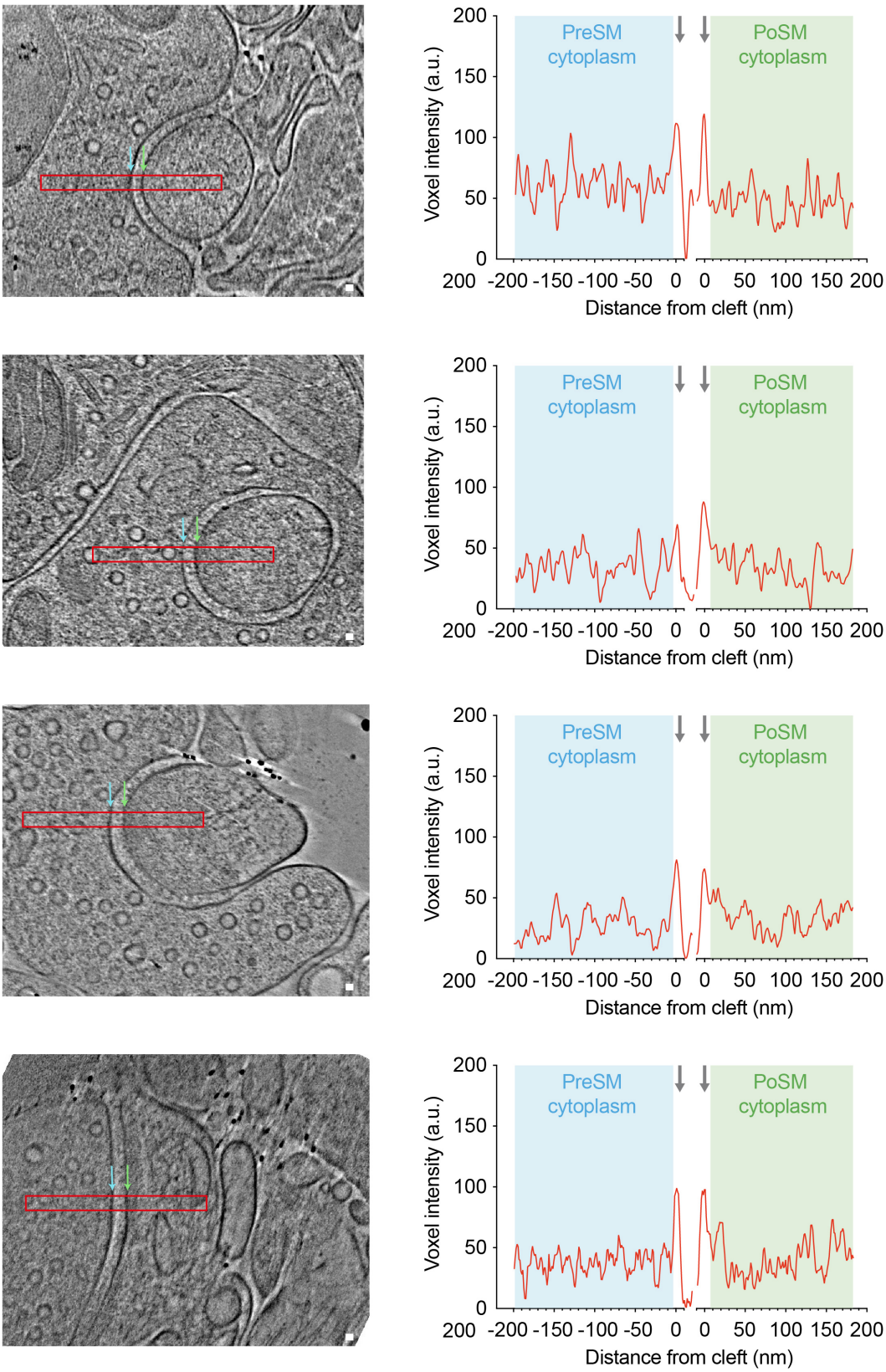

1180

Figure 1-figure supplement 3 cont.

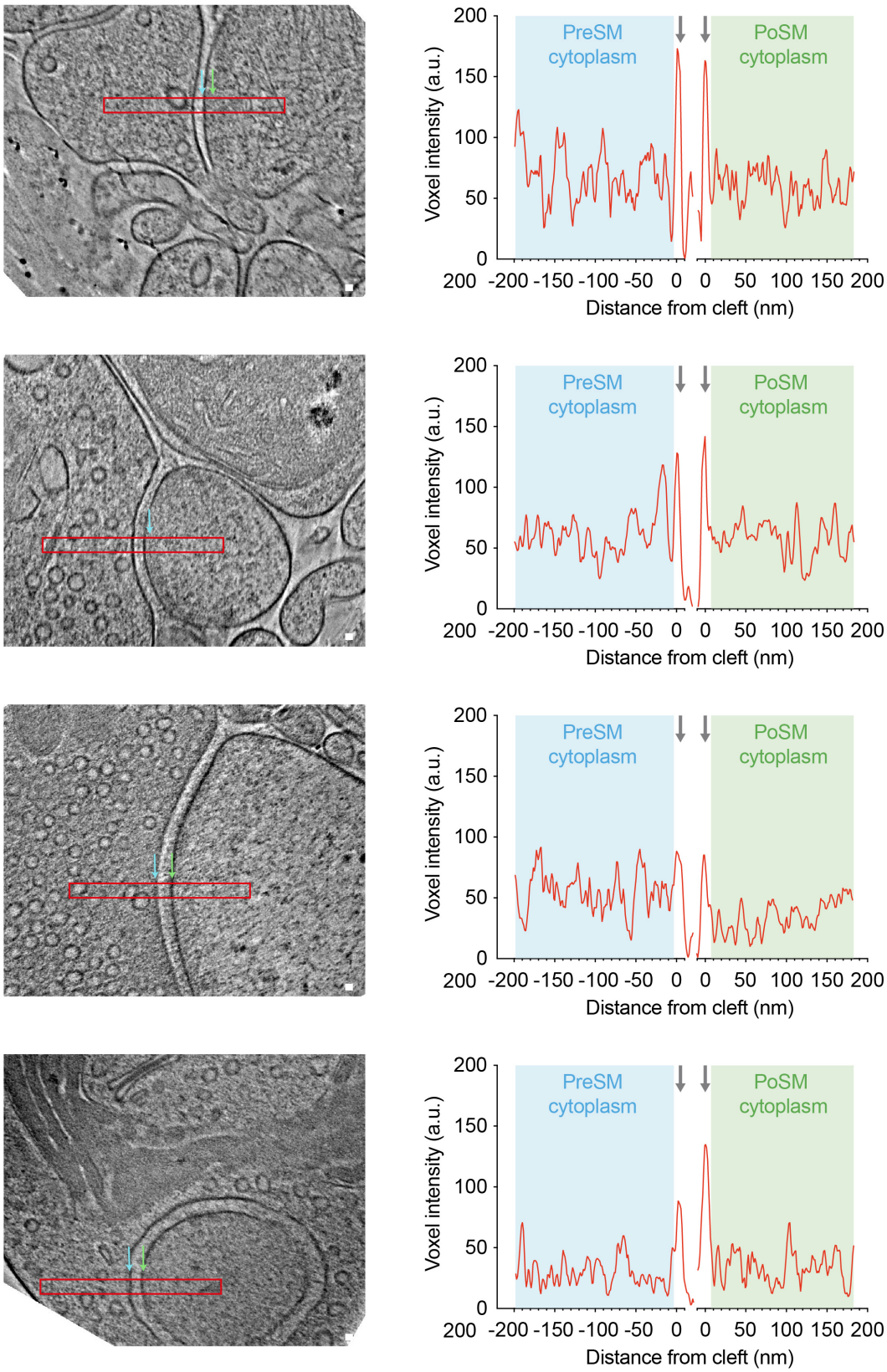

1181

Figure 1-figure supplement 3 cont.

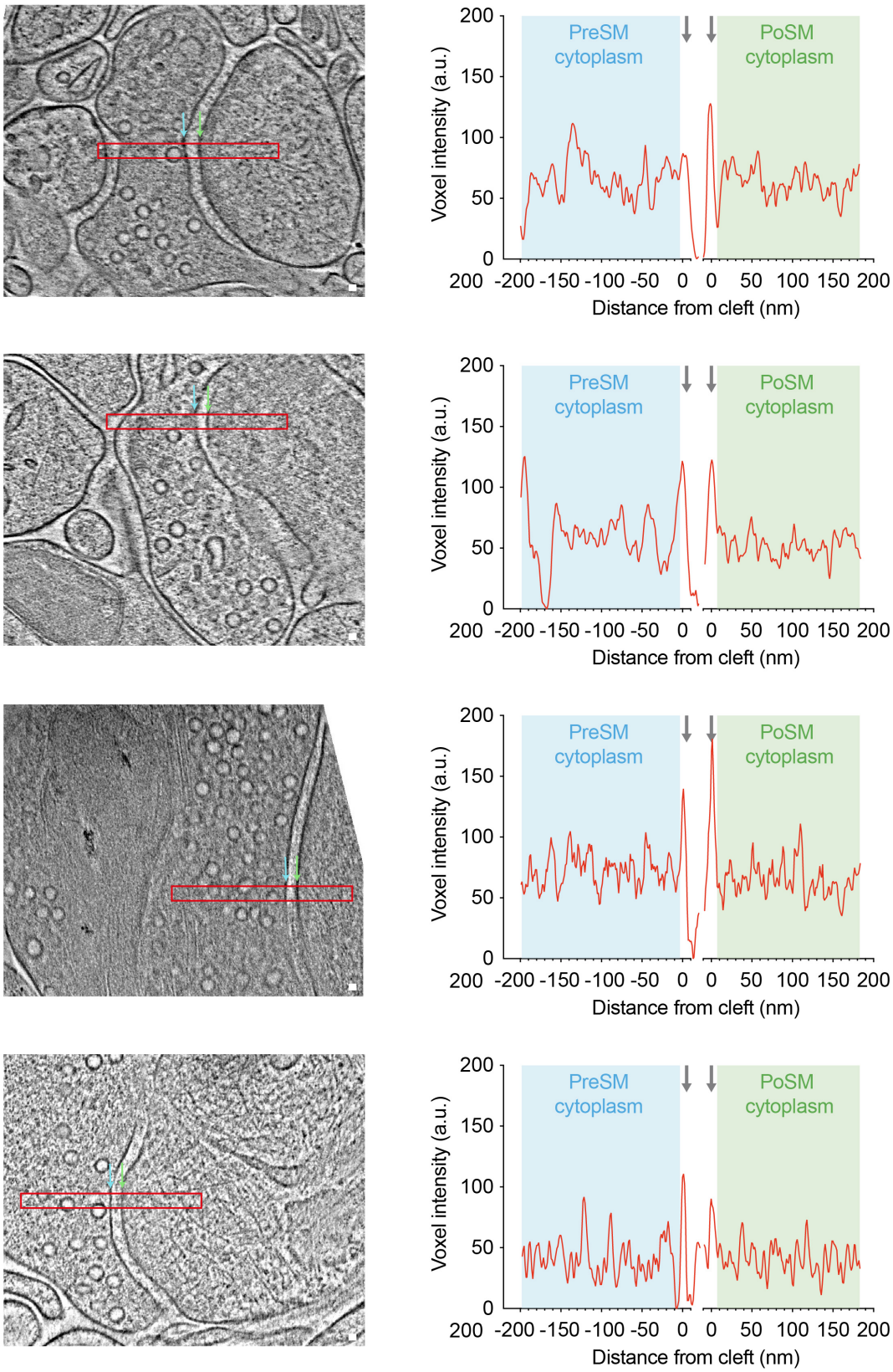

1182

Figure 1-figure supplement 3 cont.

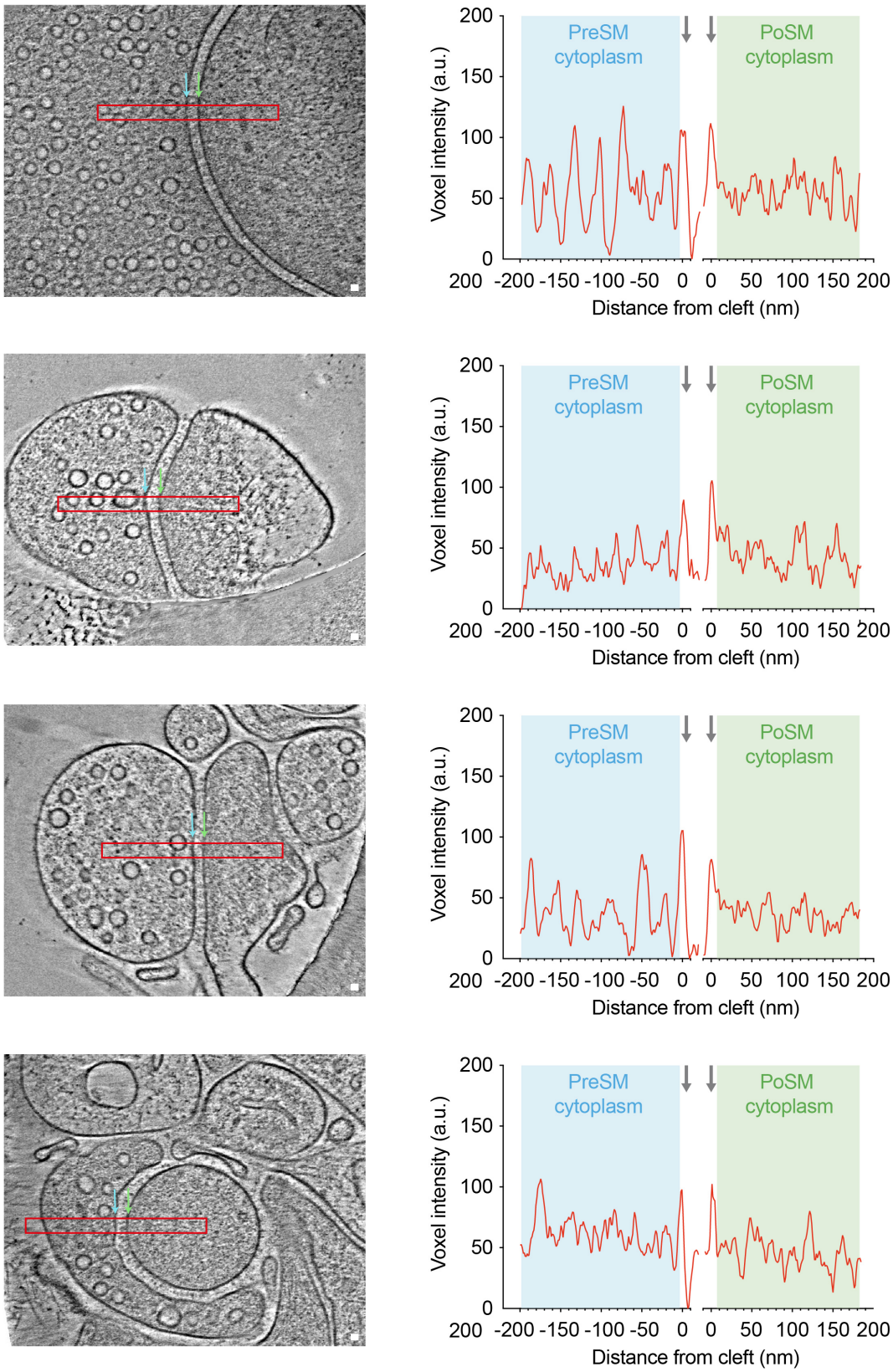

1183

Figure 1-figure supplement 3 cont.

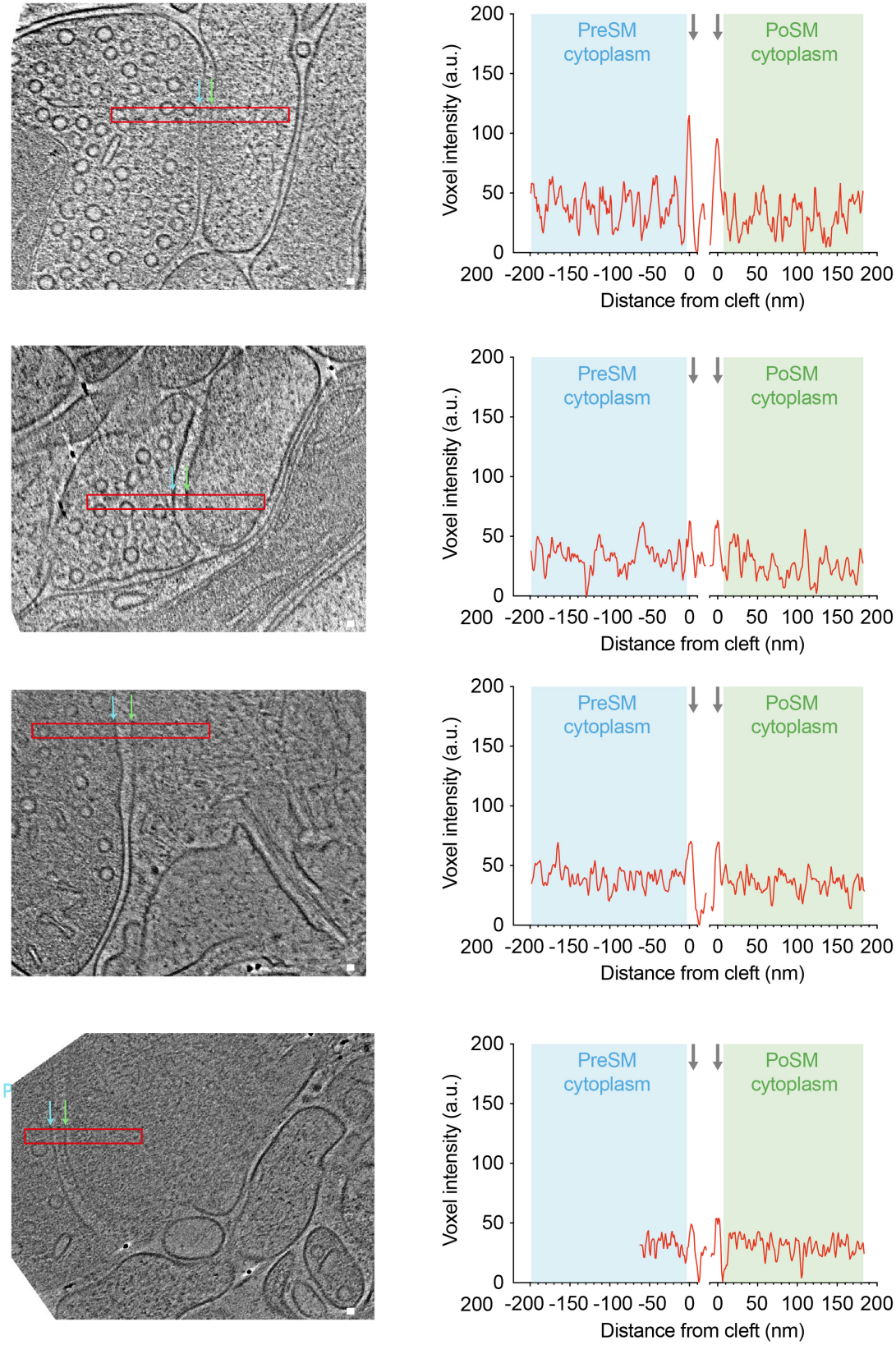

1184

Figure 1-figure supplement 3 cont.

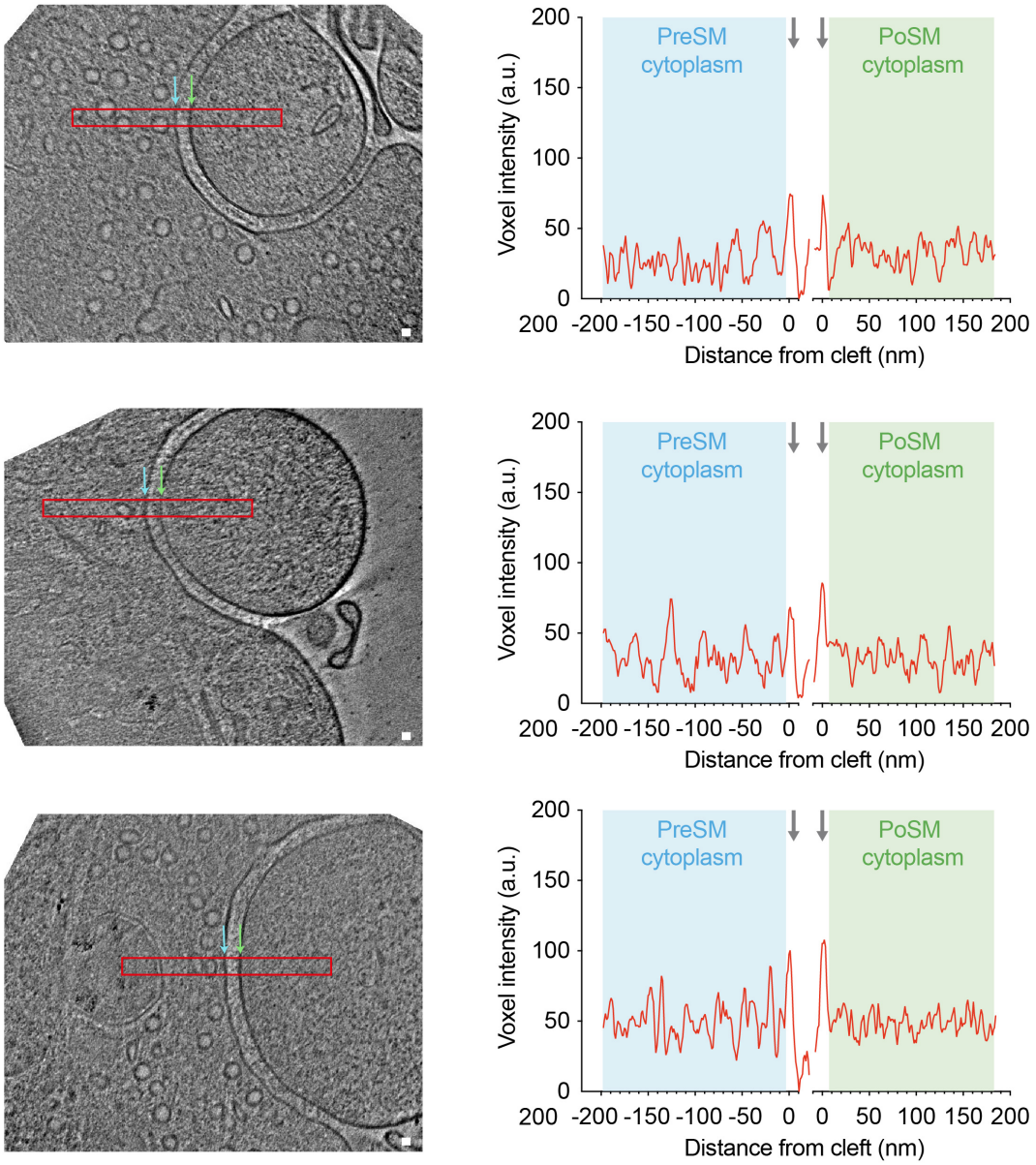

1185

1186 **Figure 1–figure supplement 3.** Tomographic slices and molecular density profiles of 27 ultra-
1187 fresh PSD95-GFP synapses. All tomograms within the ultra-fresh synapse dataset are shown in
1188 which the synaptic cleft is approximately parallel to the beam (PreSM and PoSM perpendicular to
1189 the *x-y* plane to enable accurate profile measurements of molecular density), and PoSM and PreSM
1190 compartments were closed. *Left*, tomographic slice at central regions of synaptic cleft. Red
1191 rectangle, region from which profile measuring voxel density were plotted. Scale bar, 20 nm. *Right*,
1192 average molecular density profile (36 nm wide and 450 nm long) was measured at central region
1193 of the cleft, close to docked synaptic vesicles and clusters of putative ionotropic glutamate

1194 receptors, because this is where one would expect to identify a postsynaptic density. Profiles were
1195 aligned to the lipid membrane peak of the PreSM and PoSM (grey arrows). Voxel intensity (a.u.,
1196 arbitrary units) profile plot of presynaptic (cyan) and postsynaptic (green) cytoplasm. Profiles show
1197 that the appearance of high molecular density corresponding to a PSD is not conserved in these
1198 samples compared to synapse imaged by conventional EM (see **Figure 2G-H** and **Figure 2–figure**
1199 **supplement 2**).

Figure 2-figure supplement 1

A

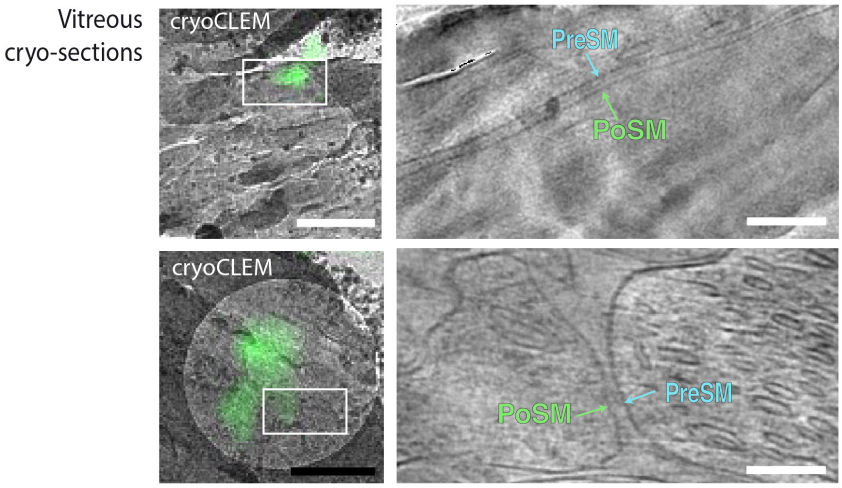

B

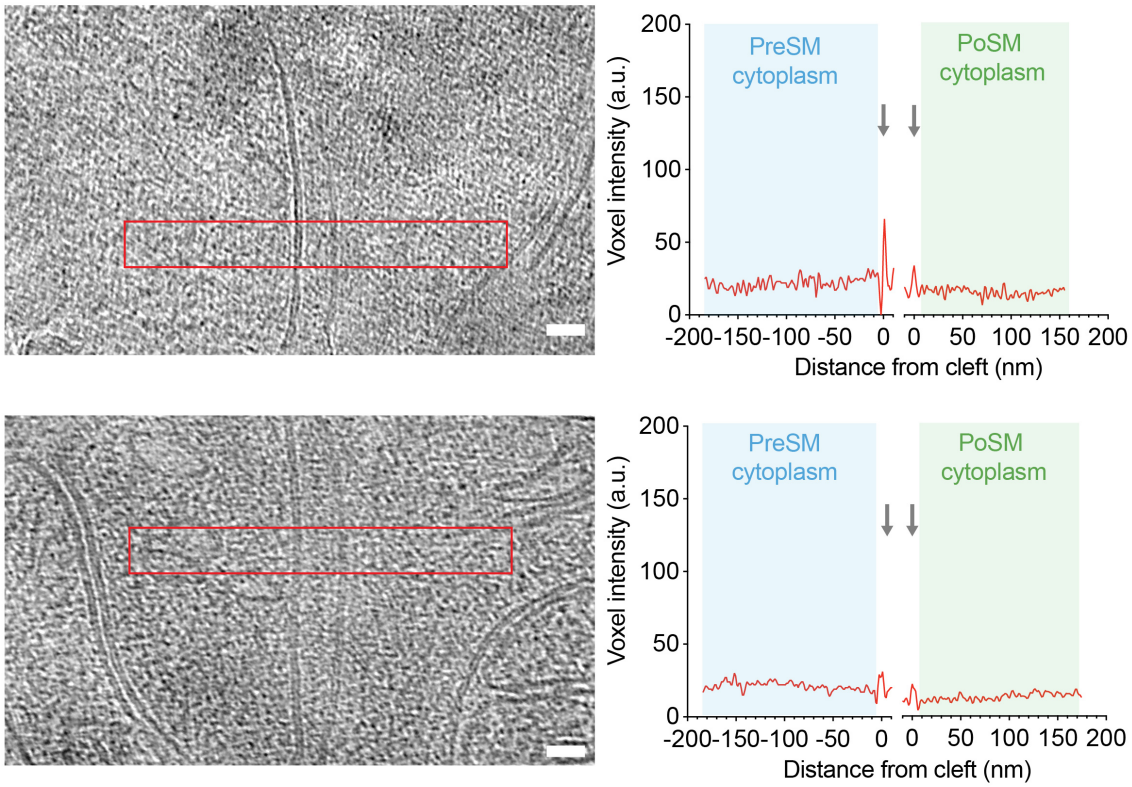

1200

Figure 2-figure supplement 1 cont.

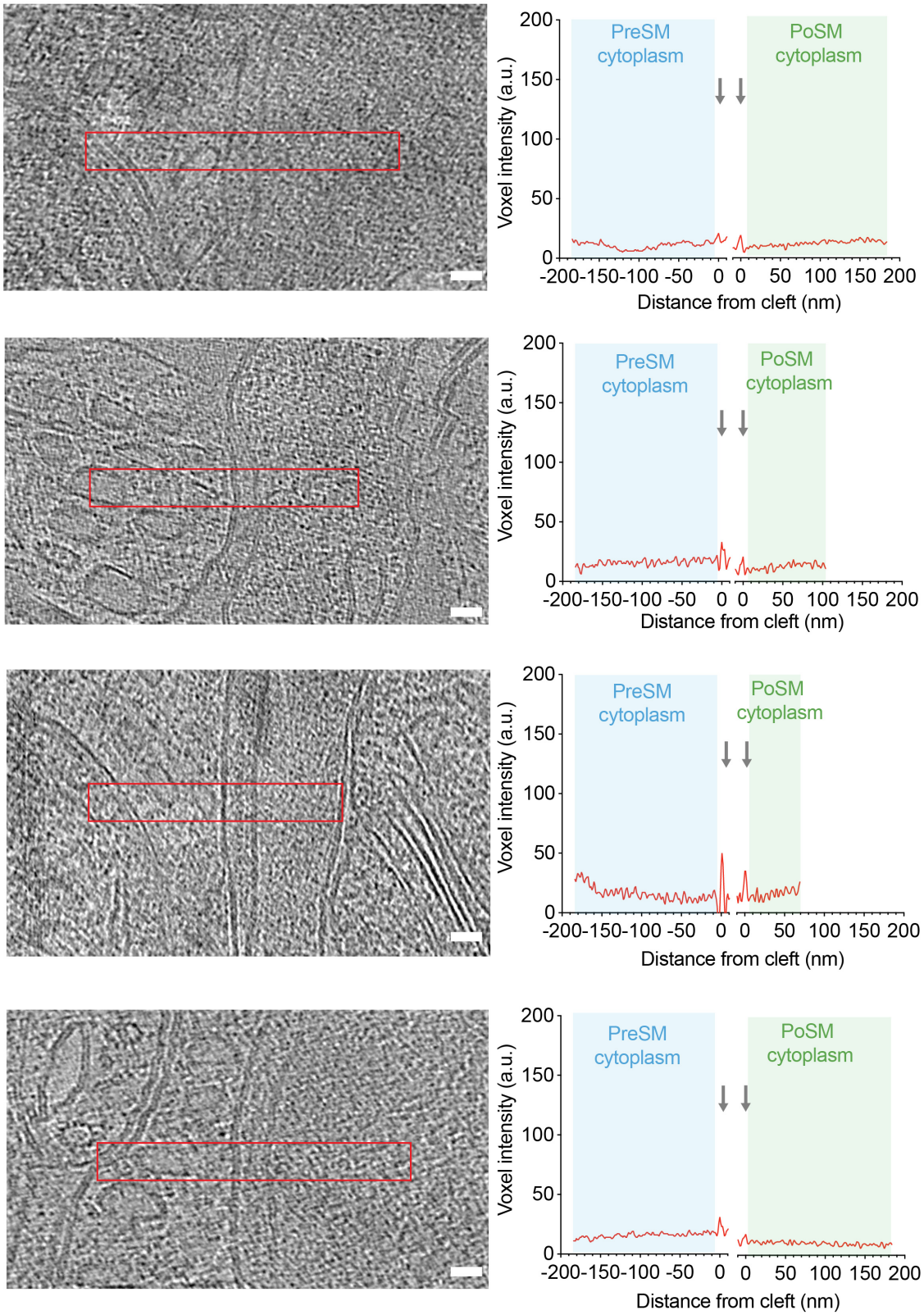

1201

Figure 2-figure supplement 1 cont.

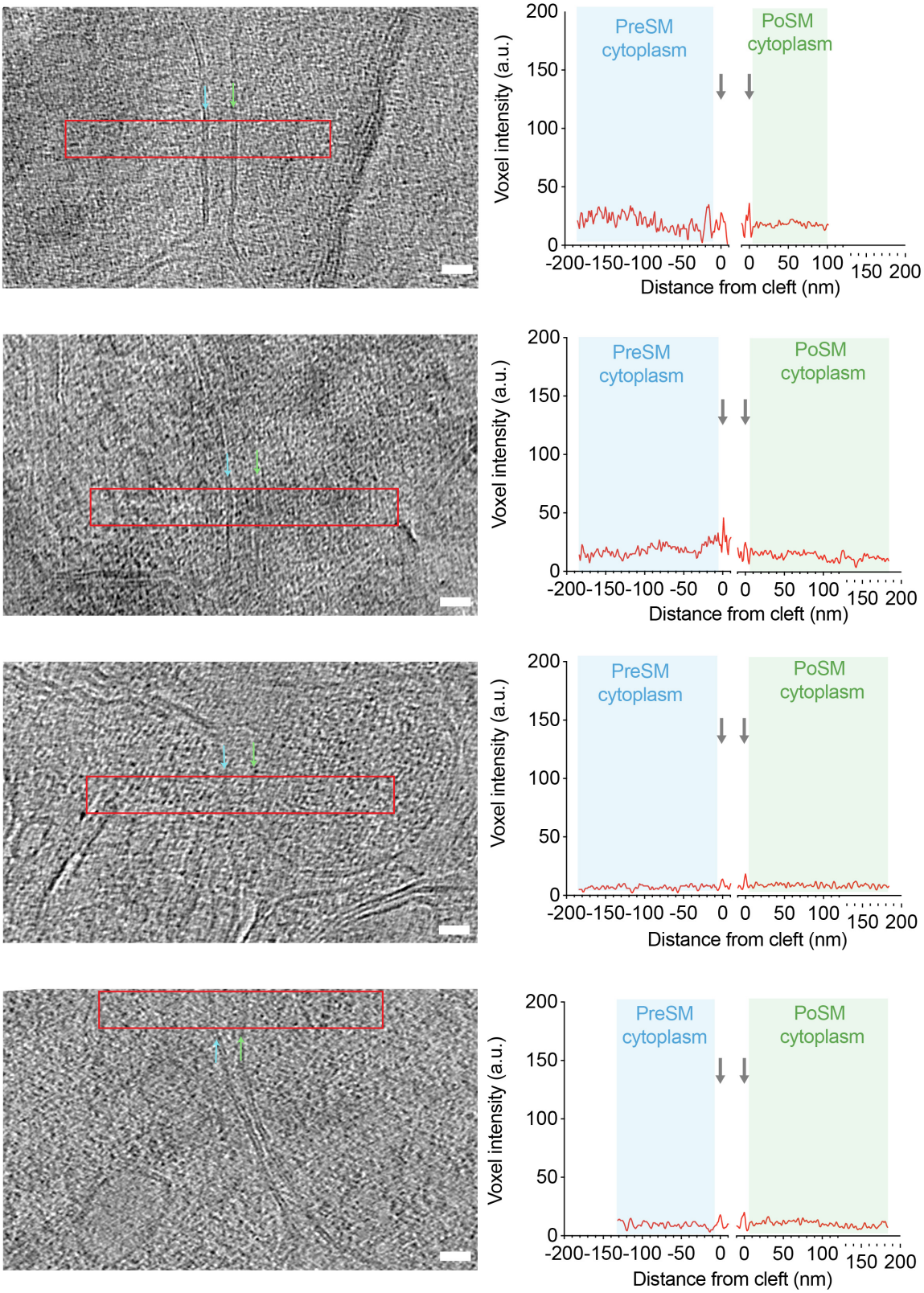

1202

Figure 2-figure supplement 1 cont.

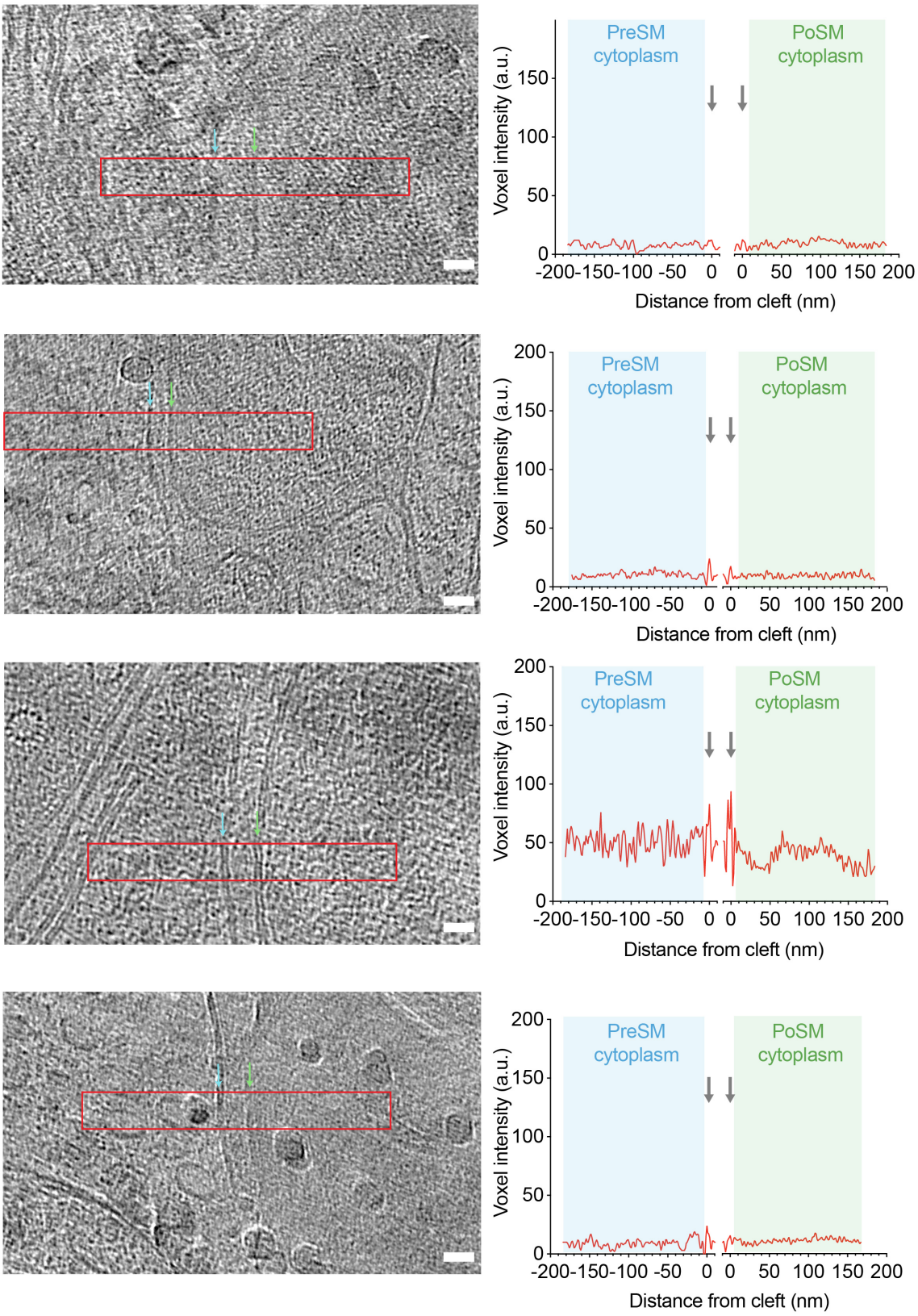

1203

Figure 2-figure supplement 1 cont.

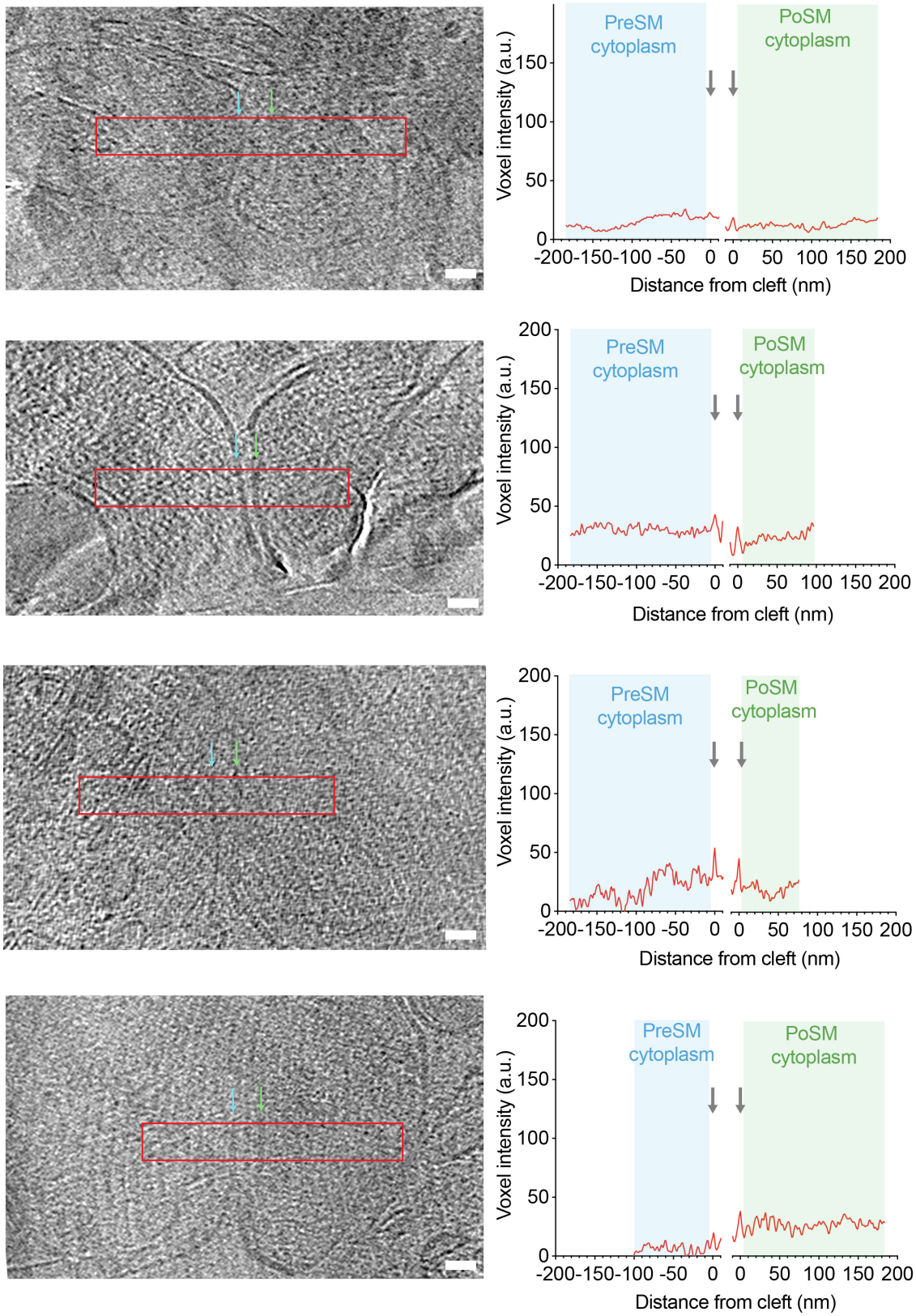

1204

Figure 2-figure supplement 1 cont.

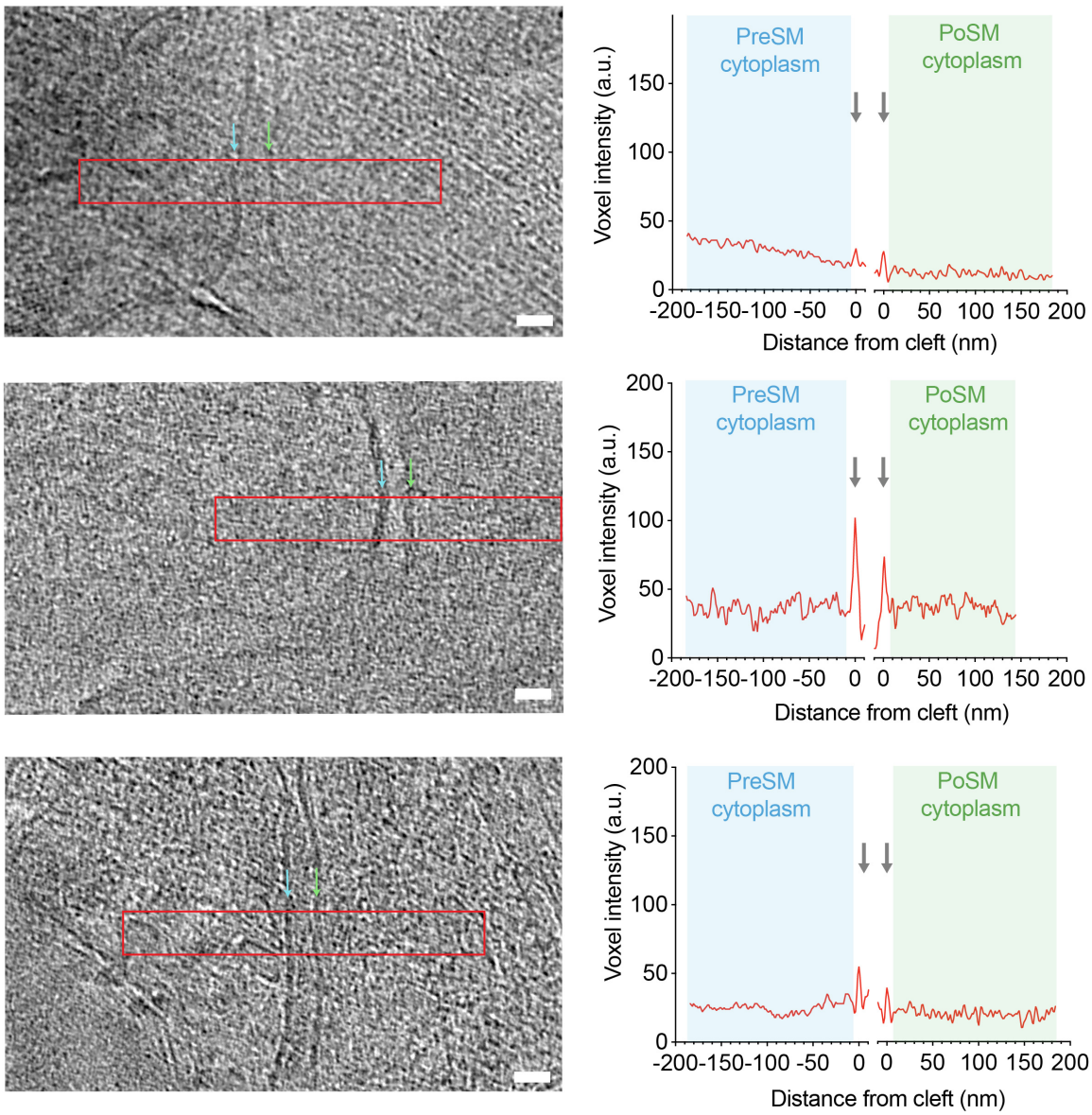

1205

1206 **Figure 2–figure supplement 1.** Molecular density profiling and tomographic slices of 21 in-tissue
1207 vitreous cryo-section tomograms containing PSD95-GFP synapses.

1208 (a) CryoCLEM and cryoET of two synapses in vitreous cryo-sections collected from adult
1209 *Psd95*$^{GFP/GFP}$ knockin mouse cortex. *Left,* PSD95-GFP cryoCLEM image of in-tissue synapse.
1210 Scale bar, 500 nm. White box, field of view in *right*, tomographic slice of PSD95-GFP
1211 containing synapse within thin vitreous cryo-section of adult mouse cortex. Cyan, PreSM.
1212 Green, PoSM. Scale bar, 50 nm. See also **Figure 2–video 2**.

1213 (b) Tomographic slices and molecular density profiles of 21 in-tissue PSD95-GFP synapses. All
1214 tomograms within the in-tissue synapse dataset are shown in which the synaptic cleft is
1215 approximately parallel to the beam (PreSM and PoSM perpendicular to the *x*-*y* plane to enable
1216 accurate profile measurements of molecular). *Left*, tomographic slice at central regions of synaptic
1217 cleft. Red rectangle, region from which profile measuring voxel density were plotted. Scale bar, 20
1218 nm. *Right*, Average molecular density profile (36 nm wide and 450 nm long) was measured at
1219 central region of the cleft, close to docked synaptic vesicles and clusters of putative ionotropic
1220 glutamate receptors, because this is where one would expect to identify a postsynaptic density.
1221 Profiles corresponding to a 37 nm sub-volume were aligned to the lipid membrane peak of the
1222 PreSM and PoSM (grey arrows). Voxel intensity (a.u., arbitrary units) profile plot of presynaptic
1223 (cyan) and postsynaptic (green) cytoplasm. Profiles show that the appearance of high molecular
1224 density corresponding to a PSD is absent in these samples compared to synapse imaged by
1225 conventional EM (see **Figure 2G-H** and **Figure 2–figure supplement 2**).

Figure 2-figure supplement 2

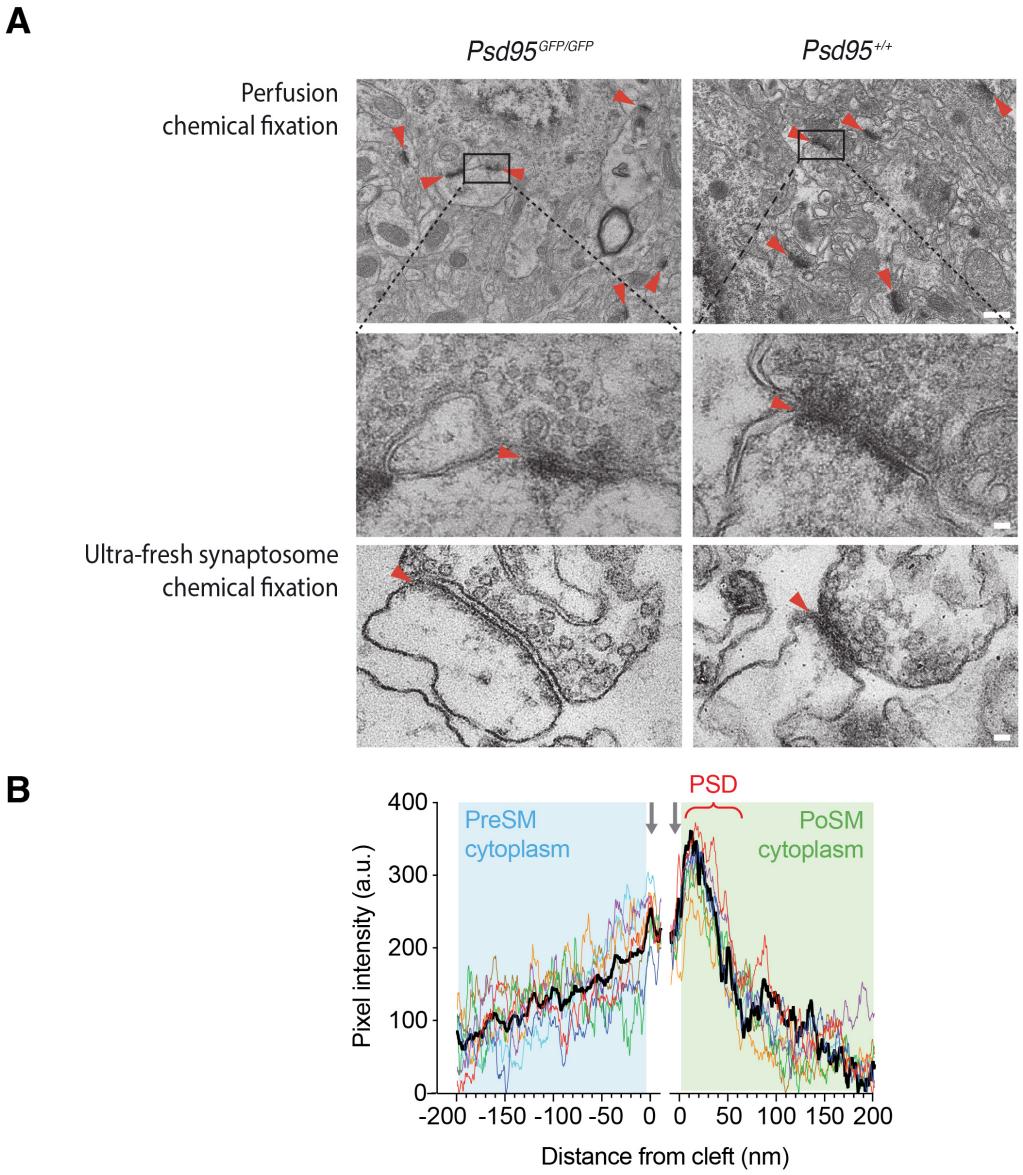

Figure 2–figure supplement 2. Conventional EM of adult brain glutamatergic synapses.

(A) Conventional EM of synapses in, resin-embedded, heavy metal-stained *Psd95*$^{GFP/GFP}$ knockin (left) and wildtype (right) mouse. Red arrowhead, postsynaptic density. Scale bar, 50 nm. *Top,* Electron micrograph showing multiple post-synaptic densities (PSDs, red arrowheads) from perfusion fixed cortex. Scale bar, 500 nm. Black box, PSD shown in *middle* close up. *Bottom*, Conventional EM of ultra-fresh forebrain synapses chemically fixed for conventional EM. Scale bar, 50 nm.

1234 (B) Molecular crowding of the PreSM and PoSM cytoplasm of perfusion fixed *Psd95*$^{GFP/GFP}$
1235 knockin mouse cortex. Pixel intensity (a.u., arbitrary units) profile plots of presynaptic (cyan) and
1236 postsynaptic (green) cytoplasm. Profiles were aligned to the lipid membrane peak of the PreSM
1237 and PoSM (grey arrows). The average intensity profile of 9 synapse tomograms is shown in black.
1238 PSD, postsynaptic density.

Figure 3-figure supplement 1

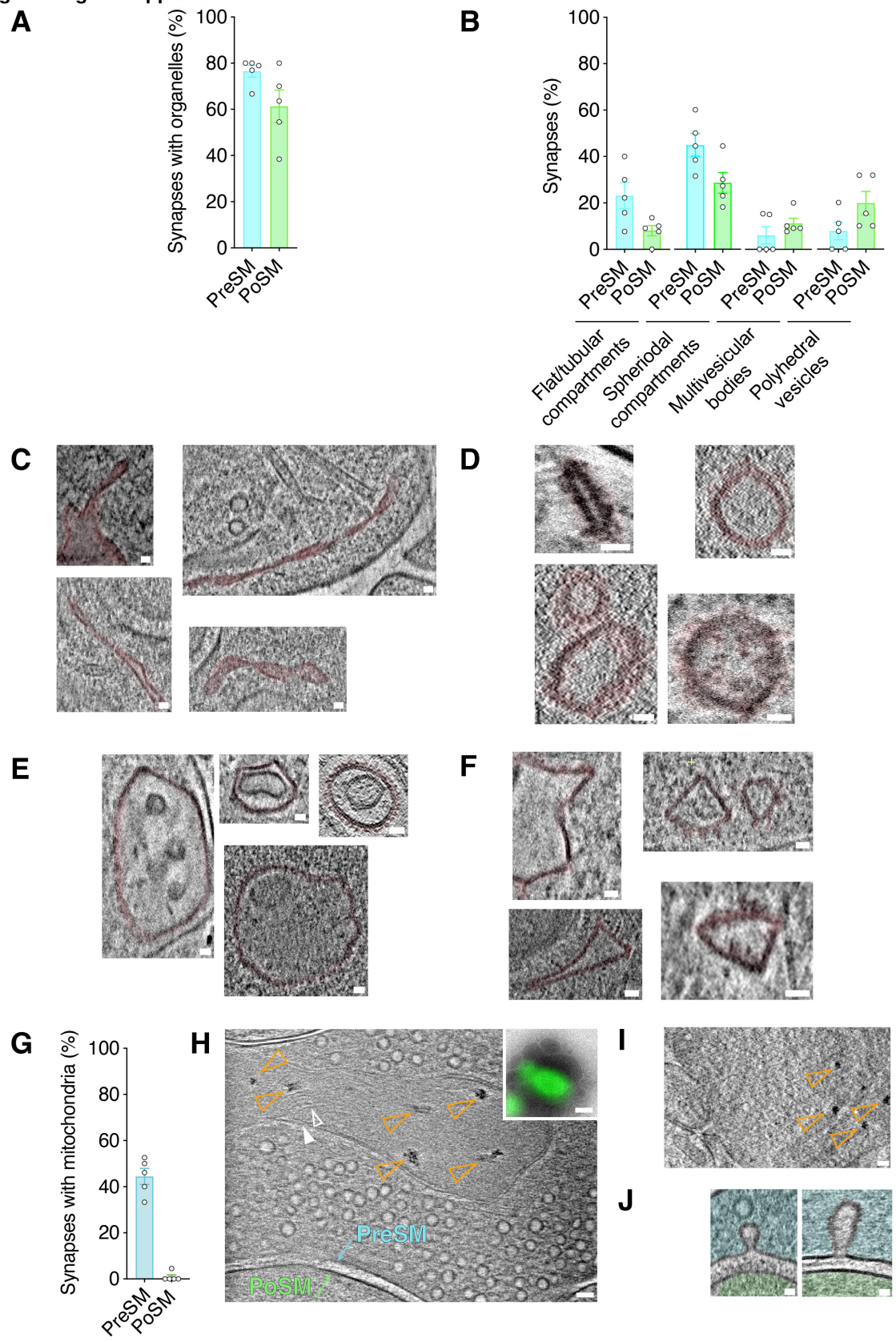

1239

1240 **Figure 3–figure supplement 1.** Structural categories of membrane-bound organelles in PSD95-
1241 containing synapses in the adult brain.

1242 (A) Prevalence of membrane bound organelles within the PreSM (cyan) and PoSM (green)
1243 compartments identified in tomograms of forebrain PSD95-GFP containing synapses from 5 adult
1244 *Psd95*$^{GFP/GFP}$ mice. Error bars, SEM.

1245 (B) Prevalence of structural classes of membrane-bound organelles, including polyhedral vesicles,
1246 flat/tubular membrane compartments, large spheroidal membrane compartments (>60 nm
1247 diameter), multivesicular bodies, and polyhedral vesicles within the PreSM (cyan) and PoSM
1248 (green) compartments of PSD95-containing forebrain synapses from 5 adult *Psd95*$^{GFP/GFP}$ mice.
1249 Error bars, SEM.

1250 (C-F) Classification of membrane-bound organelles in PSD95-GFP-containing synapses. Gallery
1251 of tomographic slices showing intracellular organelle subtype (pseudo-coloured magenta) of four
1252 different PSD95-GFP containing synapses of

1253 (C) Flat tubular twisted membranes.

1254 (D) Clustered membrane proteins in vesicles.

1255 (E) Multivesicular bodies.

1256 (F) Polyhedral membranes.

1257 Scale bar, 20 nm

1258 (G-I) Synaptic mitochondria.

1259 (G) Bar chart showing the prevalence of mitochondria in the pre- (PreSM) and post-synaptic
1260 membrane (PoSM) compartments of glutamatergic synapses.

1261 (H) Tomographic slice of synapse located by PSD95 cryoCLEM showing PreSM containing
1262 mitochondria identifiable by surrounding outer membrane (solid white arrowhead) and inner cristae
1263 membrane (open white arrowhead). Electron-dense deposits in the mitochondrial matrix are
1264 indicated with open orange arrowheads. Scale bar, 50 nm. *Top inset*, PSD95-GFP cryoCLEM
1265 image of synapse. Scale bar, 500 nm.

1266 (I) Same as h, except ultra-fresh synapses (see Methods) were prepared with ACSF omitting
1267 calcium chloride. Electron dense deposits within mitochondrial matrix were detected in all (3 out
1268 of 3) PreSM compartments. Scale bar, 50 nm.

1269 (J) Tomographic slices of synapses with intermediates of vesicle fusion/fission on the presynaptic
1270 side of the cleft of a PSD95-GFP containing synapse. *Left,* small intermediate. *Right,* Large
1271 intermediate. Scale bar, 20 nm.

Figure 4-figure supplement 1

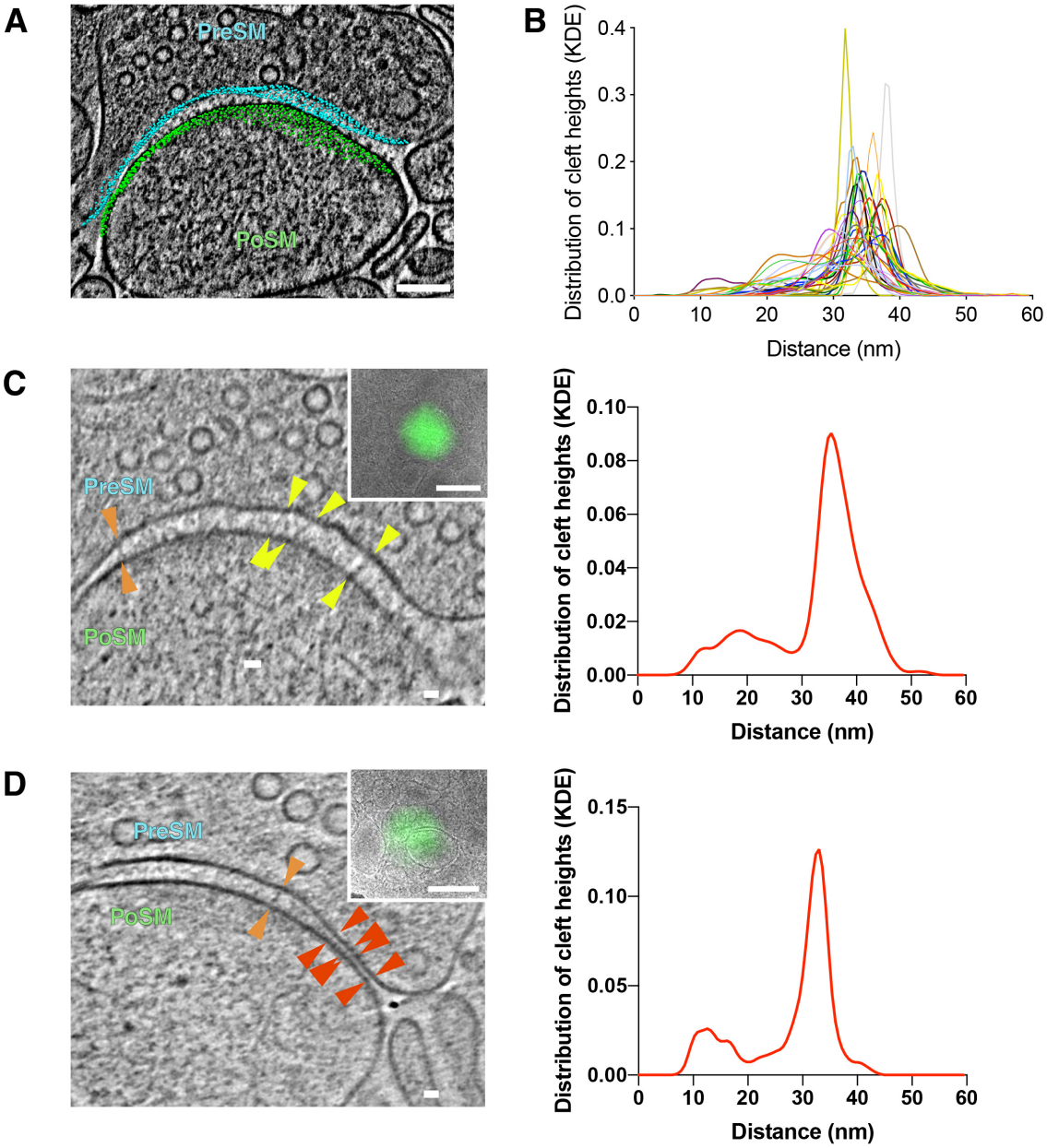

Figure 4–figure supplement 1. Quantification and variability of cleft height in glutamatergic synapses.

(A) Tomographic slice of PSD95-GFP containing synapse. 3D model of computationally determined coordinates of synaptic cleft are shown with presynaptic and postsynaptic cleft membrane coordinates depicted in cyan and green, respectively. Scale bar, 100 nm.

1278 (B) Measuring the nearest neighbour distance between presynaptic and postsynaptic coordinates of
1279 the cleft were used to quantify the cleft heights for each synapse. The distribution of cleft height
1280 distances is shown using kernel density estimation (KDE) plotted with a different colour for each
1281 synapse.

1282 (C and D) Synapses with a bimodal distribution of cleft hights. *Left*, tomographic slice of PSD95-
1283 GFP containing synapses showing subsynaptic regions with varying cleft height between PreSM
1284 (cyan) and PoSM (green). Red arrowheads, 5-15 nm transsynaptic adhesion complexes. Orange
1285 arrowheads, 22-28 nm transsynaptic adhesion complexes. Yellow arrowheads, 32-36 nm
1286 transsynaptic adhesion complexes. Scale bar, 20 nm. *Top inset*, PSD95-GFP cryoCLEM image of
1287 synapse. Scale bar, 500 nm. *Right*, the corresponding distribution of cleft height distance for each
1288 synapse is plotted using kernel density estimation (KDE).

Figure 4-figure supplement 2

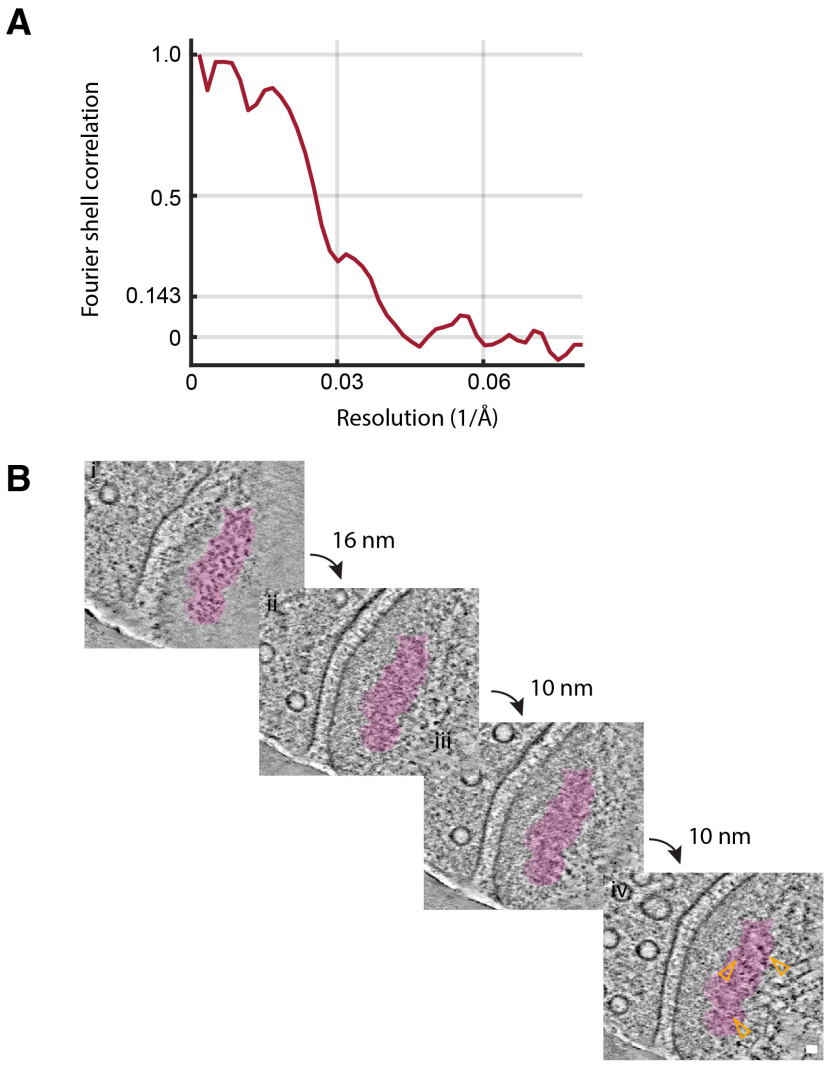

Figure 4–figure supplement 2. Subtomogram averaging and anchoring of ionotropic glutamate receptors.

(A) Estimation of the resolution of subtomogram averaged ionotropic glutamate receptors shown by plotting with a linear scale the resolution (*x*-axis) versus global Fourier shell correlation (*y*-axis).

(B) Cytoplasmic anchoring of perisynaptic ionotropic glutamate receptor clusters (pseudo-coloured in magenta). Cluster was defined using DBSCAN. Tomographic slices through tomogram of PSD95-GFP containing postsynaptic compartment. Slices separated by 16, 10, 10 and 10 nm, showing top-down views of i) extracellular membrane protein domains, ii) proximal and iii) distal

1298 cytoplasmic macromolecular complexes, iv) associated branched F-actin network (orange open
1299 arrowhead). Scale bar, 20 nm.